nature cell biology

Intraflagellar transport delivers tubulin isotypes to sensory cilium middle and distal segments

Limin Hao[1], Melanie Thein[1], Ingrid Brust-Mascher[1], Gul Civelekoglu-Scholey[1], Yun Lu[2], Seyda Acar[1], Bram Prevo[1,3], Shai Shaham[2] and Jonathan M. Scholey[1,4]

Sensory cilia are assembled and maintained by kinesin-2-dependent intraflagellar transport (IFT). We investigated whether two *Caenorhabditis elegans* α- and β-tubulin isotypes, identified through mutants that lack their cilium distal segments, are delivered to their assembly sites by IFT. Mutations in conserved residues in both tubulins destabilize distal singlet microtubules. One isotype, TBB-4, assembles into microtubules at the tips of the axoneme core and distal segments, where the microtubule tip tracker EB1 is found, and localizes all along the cilium, whereas the other, TBA-5, concentrates in distal singlets. IFT assays, fluorescence recovery after photobleaching analysis and modelling indicate that the continual transport of sub-stoichiometric numbers of these tubulin subunits by the IFT machinery can maintain sensory cilia at their steady-state length.

Sensory cilia detect and transmit signals that control gene expression, cell behaviour and development[1]. They consist of a specialized ciliary membrane containing signalling molecules surrounding an axoneme that is differentiated longitudinally into a 'middle segment' of nine microtubule doublets, and a 'distal segment', which defines a specialized signalling domain, consisting of nine singlet microtubules that extend from the A-tubules of the doublets[2–6].

Cilia are assembled by IFT, a process discovered in *Chlamydomonas* and which involves the kinesin-2-driven movement of IFT particles from the base to the tip of the axoneme[7–12]. IFT particles are multimeric protein complexes visible by electron microscopy as 'trains'[13,14] that are proposed to deliver assembly precursors, for example tubulin, to the tips of the axoneme[15–17]. Despite the progress in studying the transport of tubulin along axons[18], the role of IFT in the delivery of tubulin subunits to their site of incorporation within axonemes remains poorly understood[16].

In *C. elegans*, two members of the kinesin-2 family cooperate to drive IFT and assemble sensory cilia on chemosensory neurons. First, IFT particles, transported by the concerted action of heterotrimeric kinesin-II and homodimeric OSM-3 (osmotic avoidance abnormal 3), build the middle segment of the axoneme. Subsequently, kinesin-II dissociates from the IFT particles, which are then moved by OSM-3 alone to assemble the distal singlet microtubules[19–22]. Significantly, the hypothesis that IFT moves tubulin subunits along these cilia has not been tested, but the use of two types of kinesin-2 motor to build specific parts of sensory cilia may be widespread. For example, in vertebrates, heterotrimeric kinesin-2 (KIF3) builds the axoneme core but homodimeric kinesin-2 (KIF17), which is targeted to cilia by the nuclear import machinery, builds distal singlets on zebrafish photoreceptors and targets signalling proteins to primary cilia[2,23,24].

The *C. elegans* community has produced a collection of mutants that affect IFT and ciliogenesis[25]. Previously, by screening such mutants for defects in the OSM-3/distal segment assembly pathway, we identified the IFT particle subcomplex B (IFT-B)-associated protein, DYF-1 (abnormal dye filling 1; also known as IFT70; ref. 26), which we propose to be an OSM-3 activator[19,27]. Here we describe three IFT-B proteins and two tubulin isoforms that are also components of this pathway. Microscopy and modelling indicate that IFT transport delivers tubulins to the distal tips of axonemal microtubules, where they become differentially localized.

RESULTS

Mutants lacking the distal segments of sensory cilia fall into two classes

On the basis of the morphology of cilia containing fluorescently tagged IFT particle proteins[19,27], the *dyf* mutants[25] were organized into five groups (Supplementary Fig. S1). Complementation tests revealed that many were allelic (for example, *ks69, qj42, qj16 and che-10*; Supplementary Fig. S2, Tables S1 and S2). We focused on *qj55, qj23*, *qj14* and *dyf-12(sa127)* (refs 27,28), the uncharacterized chemosensory

[1]Department of Molecular and Cellular Biology, University of California at Davis, One Shields Avenue, 145-B Briggs Hall, Davis, California 95616, USA. [2]Laboratory of Developmental Genetics, The Rockefeller University, 1230 York Avenue, New York, New York 10065, USA. [3]Department of Physics and Astronomy and Laser Centre, VU University, De Boelelaan 1081, 1081 HV Amsterdam, The Netherlands.
[4]Correspondence should be addressed to J.M.S. (e-mail: jmscholey@ucdavis.edu)

Received 10 August 2010; accepted 21 April 2011; published online 5 June 2011; DOI: 10.1038/ncb2268

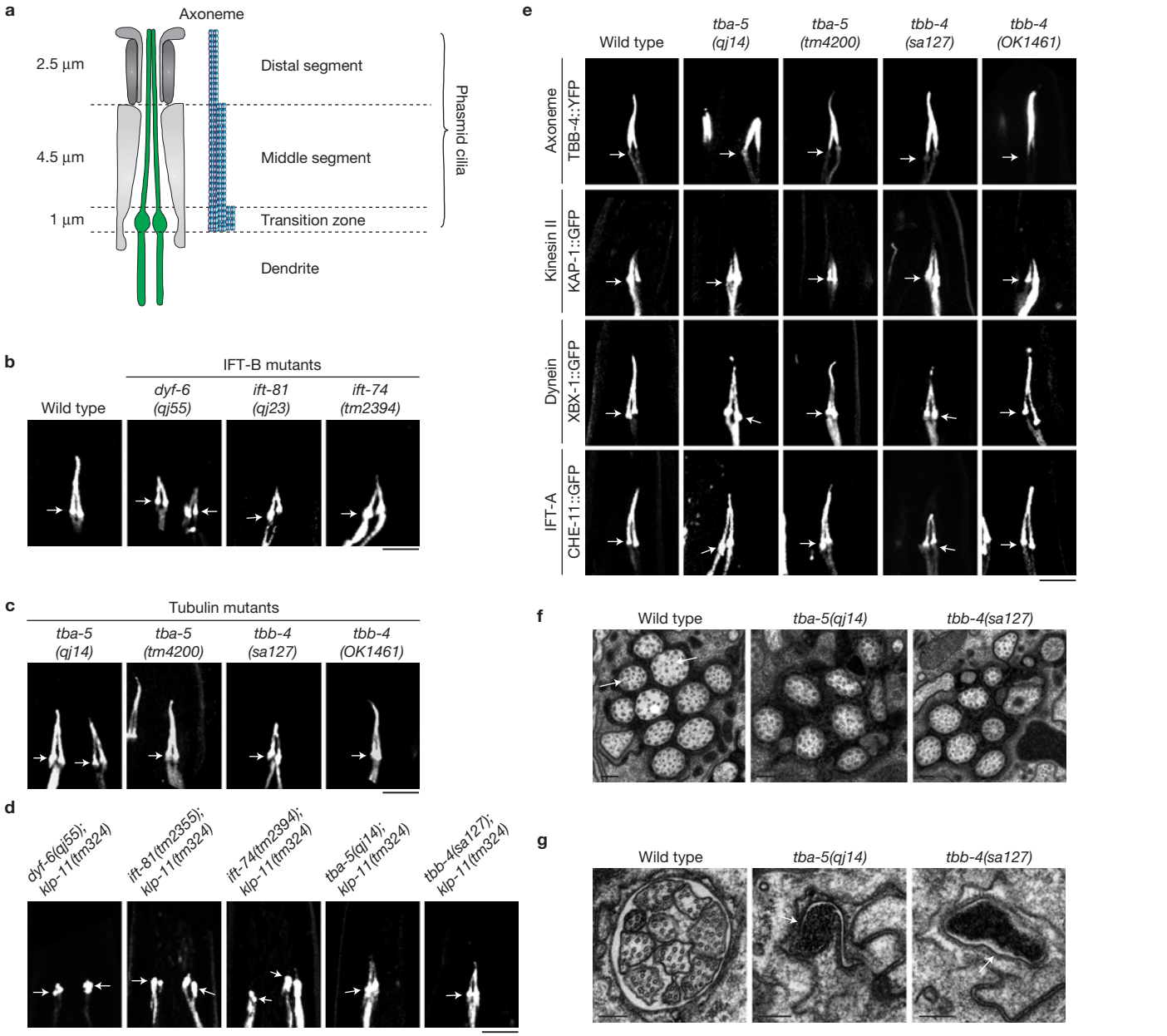

Figure 1 Characterization of the *dyf-6*, *ift-81*, *ift-74, tba-5 and tbb-4* mutants. (**a**) Schematic representation of the structure of the phasmid endings. (**b**,**c**) The DYF-1::GFP marker was used to visualize the phasmid ciliary morphology of the wild type, three IFT-B mutants (**b**) and two tubulin mutants (**c**). (**d**) The DYF-1::GFP marker was used to visualize the phasmid ciliary morphology of the double mutants, *dyf-6;klp-11*, *ift-81;klp-11*, *ift-74;klp-11*, *tba-5;klp-11* and *tbb-4;klp-11*, demonstrating that *dyf-6*, *ift-81* and *ift-74* are distinct from *tba-5(qj14)* and *tbb-4(sa127)*. (**e**) Four different markers were used to visualize the phasmid ciliary morphology in the tubulin mutants. In **b**–**e**, scale bars, 5 µm. Arrows point to transition zones with cilia oriented upward. See also Supplementary Fig. S3, which shows the ciliary morphology of these mutants in the phasmid and amphids using other markers. (**f**) Electron micrographs of amphid middle segments in wild-type (left), *tba-5(qj14)* (middle) and *tbb-4(sa127)* (right) adult animals. Arrows in the wild-type section point to singlet microtubules that occur less frequently in *tbb-4(sa127)* mutants. (**g**) Same as in **f**, except the amphid distal segment is shown. White arrows point to the empty distal channel. In **f** and **g**, scale bars, 200 nm.

mutants in class C that had intact middle segments but no distal segments (Fig. 1a–c and Supplementary Figs S1c, S3a,b and Table S3).

qj55 and *qj23* were shown to be new alleles of *dyf-6* and *ift-81*, respectively (Supplementary Table S1 and Figs S2, S4a–d; refs 29, 30), whose products, DYF-6 and IFT-81, plus the IFT-81 binding partner, IFT-74, are IFT-B subunits[13,28,29]. Double mutants *qj23;klp-11* and *qj55;klp-11*, which lack kinesin-II function, are missing the entire axoneme, similarly to the *osm-3;klp-11* mutants (Fig. 1d and Supplementary Fig. S3c and Table S3). This, together with IFT assays (Supplementary Table S4), indicates that IFT-74/81, which bound OSM-3 in yeast two-hybrid assays (Supplementary Fig. S4e), and DYF-6, which did not bind OSM-3, activate OSM-3 motor activity, similarly to the previously described IFT-B subunit, DYF-1 (ref 19; Supplementary Fig. S4f).

Although the *qj14* and *dyf-12(sa127)* mutants also lack distal segments, they define a second class of distal segment mutants, because

Table 1 Anterograde IFT velocities in the middle segment measured by IFT assays in *tba-5* and *tbb-4* and their double mutants with *klp-11(tm324)* or *bbs-8(nx77)*.

Marker	Genetic background	IFT velocity ($\mu m\,s^{-1}$)	*n*
OSM-3::GFP	Wild type	0.70±0.09	121
	tba-5(qj14)	0.78±0.09	131
	tbb-4(sa127)	0.76±0.08	146
KAP-1::GFP	Wild type	0.73±0.08	145
	tba-5(qj14)	0.74±0.10	146
	tba-5(tm4200)	0.74±0.13	118
	tbb-4(sa127)	0.75±0.09	146
	tbb-4(OK1461)	0.76±0.10	127
XBX-1::YFP	Wild type	0.77±0.08	105
	tba-5(qj14)	0.79±0.09	127
	tba-5(tm4200)	0.75±0.09	116
	tbb-4(sa127)	0.79±0.09	166
	tbb-4(OK1461)	0.79±0.10	88
CHE-11::GFP	Wild type	0.72±0.09	113
	tba-5(qj14)	0.78±0.09	210
	tba-5(tm4200)	0.74±0.08	114
	tbb-4(sa127)	0.70±0.07	116
	tbb-4(OK1461)	0.78±0.09	107
DYF-1::GFP	Wild type	0.75±0.07	155
	tba-5(qj14)	0.77±0.08	158
	tba-5(tm4200)	0.73±0.09	104
	tbb-4(sa127)	0.73±0.10	196
	tbb-4(OK1461)	0.79±0.08	117
	tba-5(qj14);klp-11	1.17±0.20	146
	tbb-4(sa127);klp-11	1.20±0.13	142
	tba-5(qj14);bbs-8	1.15±0.20	239

n indicates the number of IFT particles.

the *qj14;klp-11* or *dyf-12(sa127);klp-11* double mutants, which lack kinesin-II activity, retain intact middle segments, plausibly assembled by OSM-3-driven IFT (Fig. 1c–g and Supplementary Figs S3b,c and Table S3). In *qj14* or *dyf-12(sa127)* single mutants, IFT particles move along the residual middle segments at ~0.7 $\mu m\,s^{-1}$, characteristic of OSM-3 and kinesin-II working together, but in *qj14;klp-11* or *dyf-12(sa127);klp-11* double mutants, they move at ~1.2 $\mu m\,s^{-1}$, characteristic of OSM-3 alone (Table 1). Thus, OSM-3 retains activity and drives IFT in the *qj14* and *dyf-12(sa127)* mutants.

The second class of mutants, *qj14* and *dyf-12(sa127)*, occur in genes encoding the α- and β-tubulins, TBA-5 and TBB-4.

Complementation tests indicated that *qj14* and *dyf-10* are alleles of each other (Supplementary Fig. S2 and Table S1). Mutant *qj14* was single-nucleotide polymorphism (SNP)-mapped to the *tba-5* gene locus (Fig. 2a), which encodes one of the nine *C. elegans* α-tubulins, TBA-5. Of these, *tba-6* and *tba-9*, but not *tba-5*, were proposed to be expressed in ciliated neurons on the basis of genomic analysis[31]. SNP mapping of the mutant *dyf-12(sa127)* showed that it encodes one of the six *C. elegans* β-tubulins, TBB-4 (Fig. 2b), which is expressed in cilia[31].

Sequencing revealed that *tba-5(qj14)*, *tba-5(dyf-10)* and *tbb-4(sa127)* contain missense mutations in highly conserved residues A19V, P360L and L253F, respectively (Supplementary Fig. S5). In contrast to these mutants, the deletion mutants, *tba-5(tm4200)* and *tbb-4(OK1461)* (Fig. 2a,b) had negligible cilium defects; they were normal in dye-filling assays (Figs 2e,h and 3a), had normal cilium morphology, as assessed using TBB-4::YFP (yellow fluorescent protein) and IFT markers (Fig. 1c and Supplementary Fig. S3b), and rates of IFT along the middle segments were the same as wild type (Table 1). Thus, the deletion of TBA-5 and TBB-4 has minor effects on cilia when compared with the presence of tubulins containing the aforementioned missense mutations. As the missense mutations do not cause dominant phenotypes in genetic tests, we conclude that they are 'recessive, gain-of-function' mutations, similar to tubulin mutations causing defects in microtubule dynamics in *C. elegans* embryos[32].

To assess the impact of these distal singlet-destabilizing missense mutations, we examined their localization on TBA-5 and TBB-4 polypeptides 'docked' onto the 0.35 nm αβ-tubulin structure[33] (Fig. 2c,d). This indicates that: none of the mutated residues lies in helix H12, a main site for tubulin interaction with kinesin motors[34], concordant with them not interfering with OSM-3-driven IFT; α-tubulin mutations A19V and P360L in TBA-5 lie within helix H1 and between loops S9 and S10, respectively, which are important for proper lateral interactions between adjacent microtubule protofilaments, so these mutations may destabilize distal singlet microtubules by interfering with protofilament–protofilament interactions; and the β-tubulin mutation L253F in TBB-4 lies at the junction between loop T7 and helix H8, which contribute to longitudinal tubulin–tubulin contacts, and adjacent to a conserved lysine that may be critical for exchangeable (E)-site GTP hydrolysis[33], so this mutation may destabilize distal singlet microtubules by interfering with GTP hydrolysis and with interactions between α- and β-tubulin polypeptides.

The *tba-5* and *tbb-4* missense mutants destabilize singlet microtubules in cilia

To determine whether the missense mutations in *tba-5* and *tbb-4* destabilize distal singlet microtubules, we used dye-filling assays to monitor cilium integrity in strains cultured at 15 °C, 20 °C and 25 °C. Microtubules are destabilized at low temperatures, so we predicted that lower temperatures would cause disassembly of axoneme distal segments and defective dye filling, whereas high temperatures would stabilize them, allowing normal dye filling. DiI uptake was constant in the amphids and phasmids of wild types, both deletion strains and *tba-5(dyf-10)* at all three temperatures (Fig. 3a). However, in the missense mutants, *tbb-4(sa127)* and *tba-5(qj14)*, DiI uptake was not observed at 15 °C, consistent with the loss of cilium integrity, but dye filling increased with increasing temperature (50% amphids and 20% phasmids were stained at 25 °C). Accordingly, *tba-5(qj14)* and *tbb-4(sa127)* expressing fluorescent ciliary markers assembled only middle segments at 15 °C and full-length cilia at 25 °C (Fig. 3b,c). These results support the hypothesis that these missense mutations destabilize the singlet microtubule polymer lattice. The specific destabilization of ciliary singlet microtubules is underscored by transmission electron microscopy, which revealed loss of all distal singlet microtubules and, in the case of *tbb-4(sa127)*, loss of many central singlets in the middle segments (Fig. 1f,g).

TBA-5 and TBB-4 localize differentially within sensory cilia.

The β-tubulin *tbb-4* gene is expressed in sensory cilia in a DAF-19 (abnormal dauer formation protein 19) transcription-factor-dependent fashion[31,35]. We observed that the TBB-4::YFP protein restores the length of the cilia present on amphid (Fig. 2o) and phasmid (Fig. 2p) sensory cilia in *tbb-4(sa127)* mutants, indicating that it is functional.

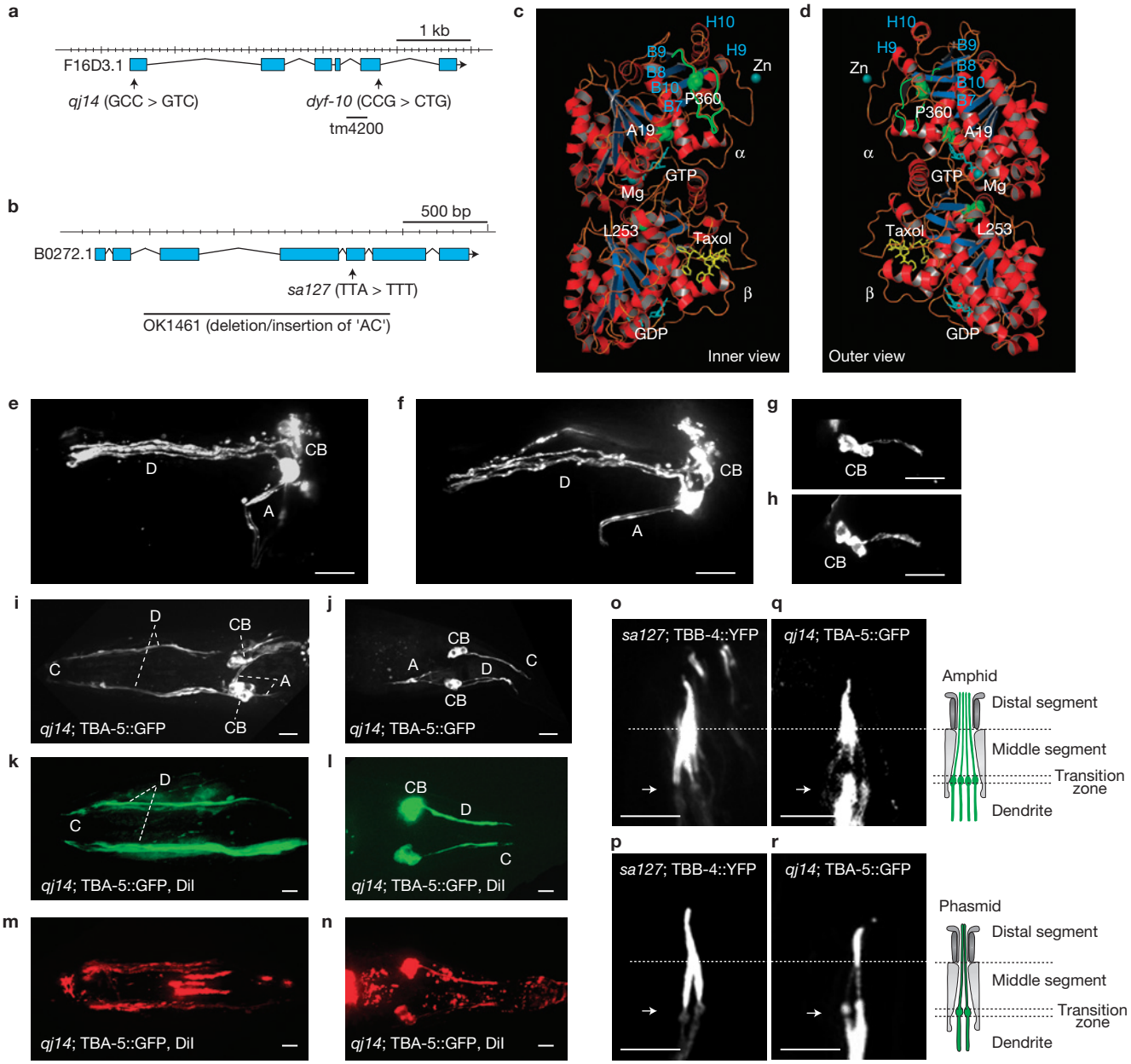

Figure 2 Expression and localization of two axonemal tubulins, TBA-5 and TBB-4, and characterization of their missense mutations. (**a**,**b**) Models of the *tba-5* and *tbb-4* gene. Two *tba-5* missense mutations, *qj14* and *dyf-10*, and a deletion mutation, *tm4200* (**a**), and a *tbb-4* missense mutation, *dyf-12(sa127)*, and a deletion mutation, *tbb-4(OK1461)* (**b**), are shown. (**c**,**d**) Inner (**c**) and outer (**d**) views of the structure of the predicted TBA-5 and TBB-4 heterodimer based on the porcine brain tubulin dimer structure, 1JFF. The three point-mutation sites (P360, A19 and L253) and the loop that contains P360 are shown in green. (**e**–**h**) Dyf assays (dye-filling assays) on *dpy-6* (**e**,**g**) and *dpy-6;tba-5(tm4200);tbb-4(OK1461)* (**f**,**h**) worms. There are no obvious defects in ciliary structure in the mutants. Scale bars, 10 μm. (**i**,**j**) A transgene *tba-5p*::*tba-5*::GFP was expressed in amphid neurons (**i**) and phasmid neurons (**j**) in *tba-5(qj14)* worms. Scale bars, 10 μm. (**k**–**n**) Cilium formation was rescued in amphids and phasmids of *tba-5(qj14)* worms by expression of the transgene, *tba-5p::tba-5::GFP*. Gene expression indicated in green in cilia and dendrites (**k**,**l**) and intact cilia shown by dyf assays (**m**,**n**; dye distribution shown in red). Scale bars, 5 μm. (**o**–**r**) TBB-4::YFP restored the ciliary length of amphids (**o**) and phasmids (**p**) in *tbb-4(sa127)* and localized to the entire cilia nearly homogeneously; TBA-5::GFP restores the lengths of amphid (**q**) and phasmid (**r**) cilia in *tba-5(qj14)* and extended from the distal regions of middle segments to the distal tips of distal segments. Scale bars, 5 μm. Right: schematic representations of the structure of the cilia and dendrites in amphids and phasmids. Arrows point to transition zones with cilia oriented upward. A, axon; C, cilia; CB, cell body; D, dendrite.

TBB-4::YFP localized along the full length of the cilium, but was not observed at the transition zone or in dendrites.

Examination of TBA-5::GFP introduced into *tba-5(qj14)* mutant worms revealed that this α-tubulin is also expressed in amphid and phasmid sensory neurons (Fig. 2i,j). TBA-5::GFP protein expression rescued the dye-filling (Fig. 2k–n) and short-cilia phenotypes of *tba-5(qj14)* mutants (Fig. 2q,r), indicating that the expressed tubulin isotype is functional. Furthermore, the tagged TBA-5 protein localized along dendrites and around the basal bodies as well as within sensory cilia. Unlike TBB-4, it was more concentrated in the distal than in the

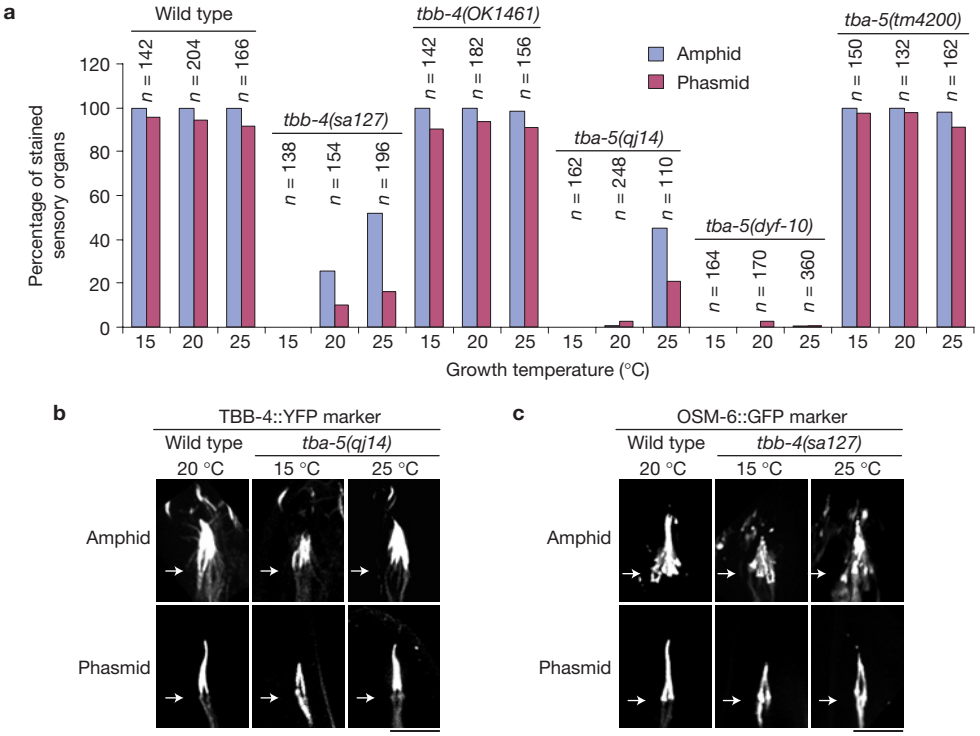

Figure 3 Tubulin point mutants are temperature sensitive. (**a**) The wild type and the two deletion mutants, *tbb-4(OK1461)* and *tba-5(tm4200)*, were nearly 100% stained in the amphid and phasmid neurons at 15 °C, 20 °C and 25 °C. *tbb-4(sa127)* and *tba-5(qj14)* worms were not stained when grown at 15 °C. However, at 25 °C, around 50% of the amphids and 20% phasmids are stained, whereas *tba-5(dyf-10)* has very little temperature effect. *n* indicates the number of amphids or phasmids. (**b**) Visualized with a TBB-4::YFP tubulin marker, *tba-5(qj14)* possessed only the middle segment of the amphid and phasmid cilia at 15 °C, but full-length cilia could be seen in *tba-5(qj14)* at 25 °C. Scale bar, 5 μm. Arrows point to transition zones with cilia oriented upward. (**c**) Visualized with an OSM-6::GFP marker, *tbb-4(sa127)* possessed only the middle segment of the amphid and phasmid cilia at 15 °C, but full-length cilia could be seen in *tbb-4(sa127)* at 25 °C. Scale bar, 5 μm. Arrows point to transition zones with cilia oriented upward. The images of the TBB-4::YFP marker in wild-type cilia in **b** and **c** is the same as used in Fig. 1e and Supplementary Fig. S3b.

middle segment within cilia, consistent with functions associated with distal singlet microtubules.

Sensory cilium microtubule plus ends exchange tubulin subunits relatively slowly at the middle and distal segment tips

We investigated the dynamics of TBB-4, which is present in both middle and distal segments of the axoneme, using fluorescence recovery after photobleaching (FRAP). Photobleaching of full-length cilia within wild-type phasmids expressing TBB-4::YFP resulted in a striking pattern of fluorescence recovery at two regions corresponding to the middle and distal segment tips and revealed that the plus ends of both the A- and B-tubules of these axonemal microtubules are dynamic (Fig. 4a). Accordingly, EBP-2::GFP, an EB1-related microtubule end-binding protein that binds polymerizing microtubule plus ends, was present at relatively high concentrations at the middle and distal segment tips, although, as in vertebrate cells, it localized all along the cilium[36] (Fig. 4f,g). Photobleaching of a TBB-4::YFP area covering only the middle (Fig. 4b) or distal (Fig. 4c) segment surprisingly revealed similar rates of recovery ($t_{1/2} = 77.2 \pm 23.7$ s, middle; 90.3 ± 20.1 s, distal). These rates were slower than in dendrites ($t_{1/2} = 4.2 \pm 2.1$ s) and were unlike those of diffusible GFP ($t_{1/2} \sim 1$–5 s) and persistently moving IFT proteins ($t_{1/2} \sim 5$–10 s), which recover all along the cilium, not only at the microtubule tips, indicating that the middle and distal segment microtubules share similar dynamic properties (Fig. 4d,e). However, the extent of recovery was higher in the distal ($42.8 \pm 18.1\%$) than in the middle ($26.7 \pm 5.6\%$) segments. As axonemal A and B tubules emanate from the transition zone with their plus ends lying at the distal (A-tubule) and middle (B-tubule) segment tips, respectively (Fig. 1A), this is consistent with turnover of A and B tubules being due to dynamic instability of their plus ends.

No EBP-2::GFP movement was detected in cilia, indicating a stable association with slowly turning over microtubule plus ends at the middle and distal segment tips, whereas robust movement of EBP-2 tracking the tips of the more dynamic dendritic microtubules was observed (see comets in Fig. 4h). In dendrites, EBP-2::GFP comets moved in both directions, consistent with an anti-parallel organization of dendritic microtubules, but most (94% out of 321 microtubules) moved from the basal body towards the cell body at $\sim 0.25 \pm 0.05\ \mu m\ s^{-1}$ (Fig. 4i), indicating that the minus ends of most of these dendritic microtubules face the cilium. Thus, we can picture the IFT machinery being moved along dynamic dendritic microtubules by minus-end-directed motors to the basal body, where the IFT proteins are unloaded, enter cilia and move along very stable axonemal microtubule tracks.

Delivery of tubulin to the tips of the middle and distal segments: IFT versus diffusion

Possible mechanisms by which tubulin subunits translocate from the transition zone to their site of incorporation at the middle and distal segment tips include passive diffusion and active transport by IFT.

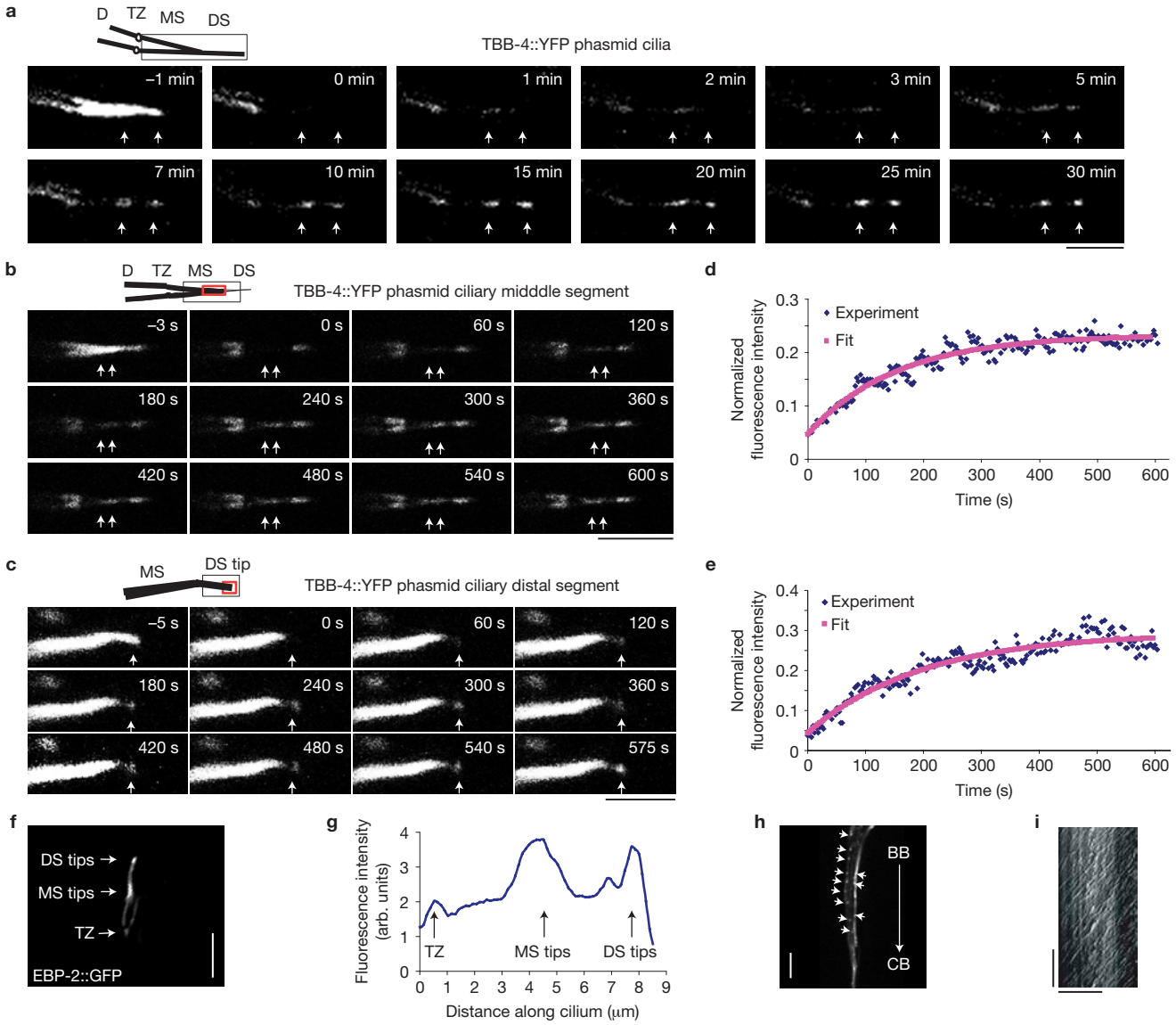

Figure 4 Dynamics of axonemal microtubules at the middle segment and distal segment tips. (**a**–**c**) Cilia expressing TBB-4::YFP were photobleached in different regions and recovery was recorded for entire cilia (**a**), tips of middle segments (**b**) and distal segments (**c**) in phasmids. In each case, images are shown before (at 0 s) and after photobleaching. The arrows point to the recovery regions. The schematic at the upper left for each set illustrates the region of cilia that was analysed; the photobleached region is shown by a black rectangle and the region used for recovery analysis is shown by a red rectangle. Scale bars, 5 μm. (**d**,**e**) The kinetics of FRAP recovery at the tips of middle segments (**d**) and the distal segments (**e**) were fitted with a single exponential equation (pink line). The fluorescence intensity is normalized to the prebleach. (**f**) EBP-2::GFP proteins are more concentrated at the tips of middle segments and distal segments. Scale bar, 5 μm. (**g**) A line scan along the cilia in **f**. (**h**) Dynamics of EBP-2::GFP in dendrites where the EB1 homologue tracks the tips of the microtubules. The arrows point to the comets. Scale bar, 5 μm. (**i**) A kymograph of EBP-2::GFP comets from **h**. Horizontal scale bar, 10 μm; vertical scale bar, 10 s. BB, basal body (equivalent to TZ); CB, cell body; D, dendrite; DS, distal segment; MS, middle segment; TZ, transition zone.

However, diffusion is inconsistent with experimental observations. GFP alone can diffuse only part of the way along the cilium and substantial amounts never reach the distal tip[37] (also our unpublished observation). Using FRAP, we estimate that GFP has a diffusion coefficient of ~1–5 $\mu m^2 s^{-1}$ in these cilia (Methods), and because GFP–tubulin is significantly larger, its diffusion coefficient must be considerably lower, indicating that tubulin could never reach the distal segment tips by diffusion alone. In contrast, tubulin could diffuse to the tip of the middle segment and a simple diffusion model would be consistent with the FRAP recovery observed at the middle segment tip (after bleach of almost the entire cilium, for example Fig. 4a), provided that enough free tubulin is available at the transition zone to maintain a concentration gradient steep enough for effective diffusion. However, an intense fluorescent TBB-4 signal at the transition zone was not observed. Moreover, this 'passive diffusion to middle segment tip' model predicts a rapid and extensive recovery all along the middle segment not just at the tips, which is not observed experimentally either (Fig. 4a).

To investigate the role of IFT in the delivery of tubulin, we compared the transport of TBB-4::YFP with that of the IFT particle component,

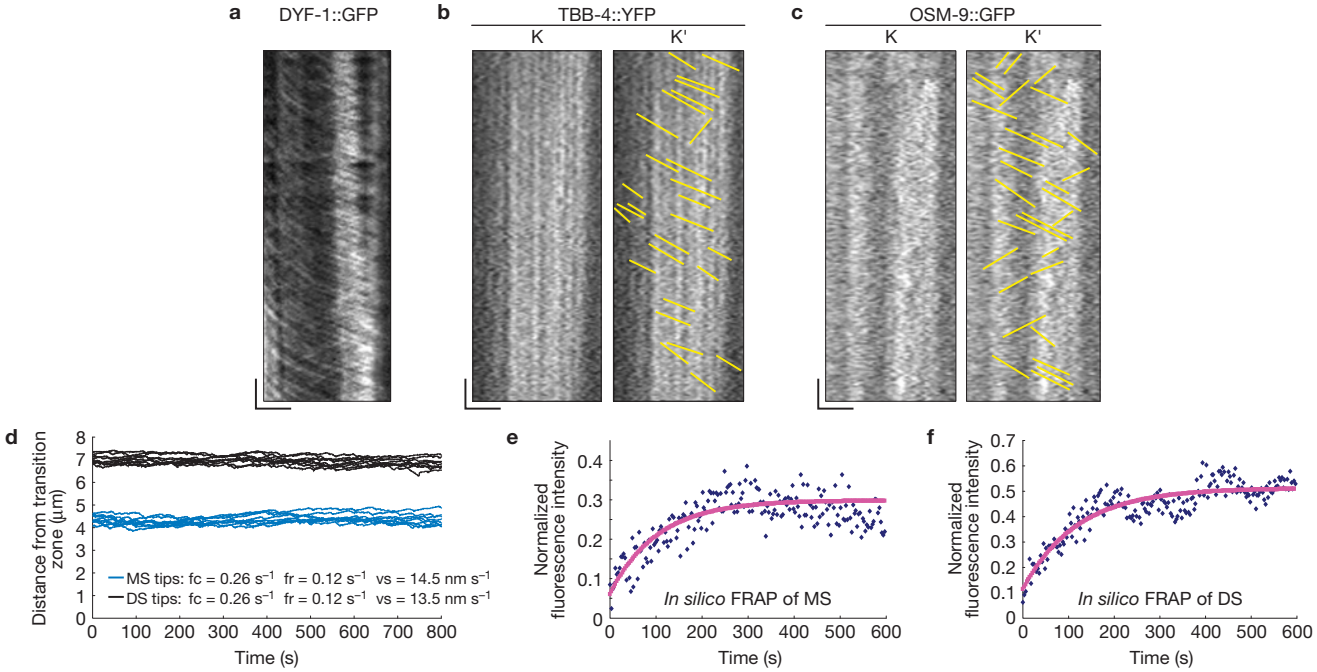

Figure 5 Analysis of TBB-4::YFP transport rate in cilia. Kymographs of DYF-1::GFP and TBB-4::YFP in IFT assays under exactly the same conditions, except that TBB-4::YFP was photobleached with a mercury lamp before recording to reduce the background. (**a**) DYF-1::GFP represents the IFT transport in cilia, and the IFT tracks are clear and thick in the kymograph. (**b**) The tracks of TBB-4::YFP in cilia are faint and thin when compared with IFT tracks, for example in **a**. (**c**) For comparison, OSM-9::GFP, which is proposed to be transported by IFT, was used as a control. All of the recorded movies were processed using the basic filters (Sharpen High and Low pass) before creating kymographs. K is the kymograph that was created along the cilia and K′ is a drawing of the kymograph lines in K. In **a**–**c**, horizontal scale bars 2.5 μm; vertical scale bars, 5 s. (**d**–**f**) Modelling of microtubule dynamics in a cilium. Dynamic instability and the delivery of tubulin subunits through IFT can constrain the length fluctuations of microtubules in both the middle (blue) and the distal (black) segments to a narrow range (**d**); *in silico* FRAP of the cilium shown in **d** for both the middle (**e**) and distal (**f**) segments indicates similar recovery curves to the experimental results (Fig. 4d,e). The fluorescence intensity is normalized to the prebleach. DS, distal segment; MS, middle segment.

DYF-1::GFP, using IFT assays. Although robust tracks of moving IFT particles were observed (Fig. 5a), tubulin movement could not be detected above the high levels of fluorescence arising from tubulin assembled into axonemes (for example, Fig. 4a). Therefore, we carried out photobleaching and looked for diagonal tracks of TBB-4::YFP moving across the bleach zone using kymography. This revealed faint diagonal tracks (Fig. 5b), similar to those seen with another presumptive IFT cargo, OSM-9 (ref. 38; Fig. 5c). The average rate of TBB-4::YFP transport was $0.8 \pm 0.1\ \mu m\ s^{-1}$ but, as with OSM-9 (ref. 38), it was not possible to discriminate characteristic middle and distal segment rates[21]. Identical results were obtained for TBA-5::GFP (data not shown). One plausible interpretation is that these transported cargoes are sub-stoichiometric to the IFT particles, which presumably bind multiple distinct molecules, so that the number of tubulin molecules per particle is much smaller than the number of IFT components per particle, but testing this requires measurement of the relevant molar ratios.

Quantitative modelling of tubulin dynamics and transport

Although consistent with a role for IFT in tubulin (and OSM-9) transport, the faint tracks seen in IFT assays are not definitive. Thus, we used modelling to determine whether active transport of tubulin by IFT could account for our tubulin FRAP data. We developed a stochastic model that describes the evolution of the doublet and singlet microtubule tips undergoing dynamic instability (that is, stochastic switches between polymerization/depolymerization), concurrent with the vectorial transport of tubulin subunits along the axoneme by IFT (Supplementary Information). Our model is derived from the deterministic balance-point model, in which the steady-state length of the axoneme is established by a balance between IFT and the turnover of axonemal tubulin subunits[16]. We investigated whether the delivery of tubulin subunits by IFT is compatible with data on: the dynamic tips being constrained to the observed narrow recovery region of less than a micrometre; the lack of fluorescence recovery everywhere along the axoneme except for the tips of the middle segment and distal segment; and the observed rate and extent of recovery of microtubule doublet and singlet tips undergoing dynamic instability (Fig. 4).

We varied the parameters of microtubule dynamic instability and the quantity of tubulin subunits transported by the IFT machinery to identify conditions that could maintain the tips within a micrometre region while also reproducing the FRAP results (half-time and per-cent recovery). We used the fewest possible parameters, only essential restrictions and the simplest assumptions to identify the minimal system compatible with the experimental data. We found parameters yielding solutions that fit the data very well in the framework of this stochastic model, so long as the variance in the number of IFT particles moving along each microtubule remains small; that is, if approximately equivalent numbers of IFT motors plus their cargo are loaded onto each microtubule at the base of the cilium, then the distal

tips of these microtubules are maintained within the experimentally observed range of one micrometre, and *in silico* FRAP of this model cilium yields recovery curves similar to those observed experimentally (Fig. 5d–f). Moreover, this good fit is obtained using rates that are characteristic of the functional cooperation between kinesin-II and OSM-3 as seen in wild-type cilia, but not using rates characteristic of either motor acting alone (Supplementary Information). We conclude that IFT driven by kinesin-II and OSM-3 in these cilia provides an efficient mechanism for maintaining microtubules at their steady-state lengths by controlling the supply of tubulin subunits such that the growth velocity is regulated and cilium length is tightly maintained in the face of microtubule dynamic instability, concordant with the balance-point model[16,17].

DISCUSSION

This screen revealed that mutants lacking distal singlets of sensory cilia fall into two classes; those disrupting OSM-3-driven IFT, including the IFT-B subunits, DYF-1 (ref. 19), DYF-6 and IFT-81/74; and those affecting microtubule tracks but not OSM-3 activity, namely missense mutations in two sensory cilium-associated α- and β-tubulin isoforms, TBA-5 and TBB-4.

Our work combined with genomics[31] identifies the α- and β-tubulins, TBA-5, TBA-6, TBA-9 and TBB-4 in sensory cilia. Of these, deletion of TBA-5 and TBB-4 yielded negligible ciliary phenotypes, indicating that they can be substituted by other tubulins. Interestingly, TBB-4 functions in all ciliated sensory neurons and distributes all along the cilium, whereas TBA-5 functions only in a subset of these cells and is more concentrated in the distal segments, indicating a functional differentiation of these tubulin isotypes within sensory cilia.

Missense mutations in TBA-5 and TBB-4 cause more severe phenotypes than the deletion mutants, similarly to missense mutations in certain vertebrate tubulin isotypes that yield stronger neurological phenotypes than RNA interference (RNAi)-mediated knockdown[39,40], and they resemble 'recessive, gain of function' missense mutations found in *C. elegans* embryos[32]. We propose that these mutations, which occur at conserved residues, may directly destabilize polymerized distal singlet and middle segment central singlet microtubules, although indirect mechanisms, for example sequestration of a chaperone required for singlet assembly, are also possible. Axoneme-specific tubulin residues such as A19 and P360 in TBA-5 and L253 in TBB-4 are proposed to be evolutionarily conserved because they are required to build specific parts of axonemes[41], in this instance because of their importance in maintaining singlet microtubules that form specific parts of sensory cilia.

We investigated how TBA-5 and TBB-4 assemble into axonemes. FRAP revealed that axonemal microtubules turn over with $t_{1/2}$ of around 1–2 min, an order of magnitude slower than dendritic microtubules in the same neurons, and incorporate tubulin subunits at the plus ends of both the A-tubule (at distal segment tip) and the B-tubule (at middle segment tip), where the growing microtubule plus-end tip tracker, EBP-2, is concentrated.

To enter the cilium, IFT proteins and their tubulin cargo must move along dendritic microtubules from the cell body to the transition zone. As most microtubules seem to be oriented with their minus ends facing the cilium, minus-end-directed microtubule motors may mediate this dendritic transport, although counterarguments include the possibility that plus-end motors could select the minor population of opposite-polarity microtubules.

IFT assay results were consistent with the hypothesis that TBA-5 and TBB-4 are transported from the base to the tip of the axoneme by IFT in amounts that are sub-stoichiometric to subunits of IFT particles and motors, which yield more robust tracks in kymographs[21,27]. Quantitative modelling supports this hypothesis by providing an excellent fit to experimental FRAP data. In the model, tubulin subunits transported along a specific microtubule can incorporate only onto the tips of the same microtubule, and to maintain all microtubule tips within the sub-micrometre region observed during FRAP recovery, we had to keep the number of IFT particles per microtubule approximately equal. An elaborate 'gated import' machinery is thought to regulate entry of IFT particles at the basal body[24,42] and could target equivalent numbers of IFT particles to each microtubule. Alternative, untested explanations for the tight microtubule length regulation observed are: tubulin subunits are unequally loaded onto microtubules at the base but following unloading at the tips, they diffuse to dissipate any tubulin accumulation and then incorporate equivalently into all microtubules as needed; or additional factors regulate microtubule dynamics to maintain their length.

The delivery of tubulin subunits to the tips of axonemal microtubules by IFT is a cornerstone of the balance-point model for cilium length control[16,17]. Our finding that a refined, stochastic version of this model can explain new experimental data on tubulin dynamics using reasonable parameters supports this hypothesis. Thus, we suggest that, reminiscent of the delivery of tubulin by axonal transport motors for axonal microtubule assembly[18], IFT motors transport tubulin subunits along axonemes to maintain sensory cilia. □

METHODS

Methods and any associated references are available in the online version of the paper at http://www.nature.com/naturecellbiology

Note: Supplementary Information is available on the Nature Cell Biology website

ACKNOWLEDGEMENTS

We thank X. Zhang (Heyer Laboratory), A. Desai and G. Ou for valuable discussion; M. Shohei (Tokyo Women's Medical University, School of Medicine, Tokyo, Japan) for the deletion mutants, *tm2355, tm2394* and *tm4200*; the *Caenorhabditis* Genetics Center (funded by the NIH National Center for Research Resources) for strains; and Y. Kohara, Center for Genetic Resource Information, National Institute of Genetics, Japan for EST clones. This work was supported by NIH grant nos GM50718 to J.M.S. and R01NS064273 to S.S.

AUTHOR CONTRIBUTIONS

J.M.S is the principal investigator of the grant and laboratory that support this IFT project. L.H. and J.M.S. designed the experiments and drafted the manuscript. J.M.S. wrote the manuscript. L.H. carried out most of the experiments. M.T. characterized the *qj14* mutant by crossing all of the used IFT markers into it, made the TBB-4::YFP transgenic worms and carried out the EBP-2 experiments. I.B-M. implemented the stochastic tubulin transport and dynamics model and the *in silico* FRAP model and analysed the results, and helped with the FRAP experiment and transport assay of TBB-4::YFP and analysis of the results. G.C-S. designed and wrote the stochastic tubulin transport and dynamics model and the *in silico* FRAP model scripts. Y.L. and S.S. carried out the electron microscopy studies and analysed the results. S.A. and B.P. carried out the Y2H assays. All of the authors read the manuscript.

COMPETING FINANCIAL INTERESTS

The authors declare no competing financial interests.

Published online at http://www.nature.com/naturecellbiology
Reprints and permissions information is available online at http://www.nature.com/reprints

1. Goetz, S. C. & Anderson, K. V. The primary cilium: a signalling centre during vertebrate development. *Nat. Rev. Genet.* **11,** 331–344 (2010).
2. Insinna, C., Pathak, N., Perkins, B., Drummond, I. & Besharse, J. C. The homodimeric kinesin, Kif17, is essential for vertebrate photoreceptor sensory outer segment development. *Dev. Biol.* **316,** 160–170 (2008).
3. Mesland, D. A., Hoffman, J. L., Caligor, E. & Goodenough, U. W. Flagellar tip activation stimulated by membrane adhesions in *Chlamydomonas* gametes. *J. Cell Biol.* **84,** 599–617 (1980).
4. Moran, D. T., Rowley, J. C. 3rd, Jafek, B. W. & Lovell, M. A. The fine structure of the olfactory mucosa in man. *J. Neurocytol.* **11,** 721–746 (1982).
5. Perkins, L. A., Hedgecock, E. M., Thomson, J. N. & Culotti, J. G. Mutant sensory cilia in the nematode *Caenorhabditis elegans*. *Dev. Biol.* **117,** 456–487 (1986).
6. Wang, Q., Pan, J. & Snell, W. J. Intraflagellar transport particles participate directly in cilium-generated signaling in *Chlamydomonas*. *Cell* **125,** 549–562 (2006).
7. Cole, D. G. *et al.* Novel heterotrimeric kinesin-related protein purified from sea urchin eggs. *Nature* **366,** 268–270 (1993).
8. Cole, D. G. *et al. Chlamydomonas* kinesin-II-dependent intraflagellar transport (IFT): IFT particles contain proteins required for ciliary assembly in *Caenorhabditis elegans* sensory neurons. *J. Cell Biol.* **141,** 993–1008 (1998).
9. Kozminski, K. G., Johnson, K. A., Forscher, P. & Rosenbaum, J. L. A motility in the eukaryotic flagellum unrelated to flagellar beating. *Proc. Natl Acad. Sci. USA* **90,** 5519–5523 (1993).
10. Shakir, M. A., Fukushige, T., Yasuda, H., Miwa, J. & Siddiqui, S. S. *C. elegans osm-3* gene mediating osmotic avoidance behaviour encodes a kinesin-like protein. *Neuroreport* **4,** 891–894 (1993).
11. Pedersen, L. B. & Rosenbaum, J. L. Intraflagellar transport (IFT) role in ciliary assembly, resorption and signalling. *Curr. Top. Dev. Biol.* **85,** 23–61 (2008).
12. Hao, L & Scholey, J. M. Intraflagellar transport at a glance. *J. Cell Sci.* **122,** 889–892 (2009).
13. Lucker, B. F., Miller, M. S., Dziedzic, S. A., Blackmarr, P. T. & Cole, D. G. Direct interactions of intraflagellar transport complex B proteins IFT88, IFT52, and IFT46. *J. Biol. Chem.* **285,** 21508–21518 (2010).
14. Pigino, G. *et al.* Electron-tomographic analysis of intraflagellar transport particle trains *in situ*. *J. Cell Biol.* **187,** 135–148 (2009).
15. Johnson, K. A. & Rosenbaum, J. L. Polarity of flagellar assembly in *Chlamydomonas*. *J. Cell Biol.* **119,** 1605–1611 (1992).
16. Marshall, W. F. & Rosenbaum, J. L. Intraflagellar transport balances continuous turnover of outer doublet microtubules: implications for flagellar length control. *J. Cell Biol.* **155,** 405–414 (2001).
17. Engel, B. D., Ludington, W. B. & Marshall, W. F. Intraflagellar transport particle size scales inversely with flagellar length: revisiting the balance-point length control model. *J. Cell Biol.* **187,** 81–89 (2009).
18. Shah, J. V. & Cleveland, D. W. Slow axonal transport: fast motors in the slow lane. *Curr. Opin. Cell Biol.* **14,** 58–62 (2002).
19. Ou, G., Blacque, O. E., Snow, J. J., Leroux, M. R. & Scholey, J. M. Functional coordination of intraflagellar transport motors. *Nature* **436,** 583–587 (2005).
20. Pan, X. *et al.* Mechanism of transport of IFT particles in *C. elegans* cilia by the concerted action of kinesin-II and OSM-3 motors. *J. Cell Biol.* **174,** 1035–1045 (2006).
21. Snow, J. J. *et al.* Two anterograde intraflagellar transport motors cooperate to build sensory cilia on *C. elegans* neurons. *Nat. Cell Biol.* **6,** 1109–1113 (2004).
22. Burghoorn, J. *et al.* Mutation of the MAP kinase DYF-5 affects docking and undocking of kinesin-2 motors and reduces their speed in the cilia of *Caenorhabditis elegans*. *Proc. Natl Acad. Sci. USA* **104,** 7157–7162 (2007).
23. Jenkins, P. M. *et al.* Ciliary targeting of olfactory CNG channels requires the CNGB1b subunit and the kinesin-2 motor protein, KIF17. *Curr. Biol.* **16,** 1211–1216 (2006).
24. Dishinger, J. F. *et al.* Ciliary entry of the kinesin-2 motor KIF17 is regulated by importin-β2 and RanGTP. *Nat. Cell Biol.* **12,** 703–710 (2010).
25. Inglis, P. N., Ou, G., Leroux, M. R. & Scholey, J. M. The sensory cilia of *Caenorhabditis elegans*. *WormBook* 1–22 (2007).
26. Fan, Z. C. *et al.* Chlamydomonas IFT70/CrDYF-1 is a core component of IFT particle complex B and is required for flagellar assembly. *Mol. Biol. Cell* **21,** 2696–2706 (2010).
27. Ou, G. *et al.* Sensory ciliogenesis in *Caenorhabditis elegans*: assignment of IFT components into distinct modules based on transport and phenotypic profiles. *Mol. Biol. Cell* **18,** 1554–1569 (2007).
28. Kobayashi, T., Gengyo-Ando, K., Ishihara, T., Katsura, I. & Mitani, S. IFT-81 and IFT-74 are required for intraflagellar transport in *C. elegans*. *Genes Cells* **12,** 593–602 (2007).
29. Bell, L. R., Stone, S., Yochem, J., Shaw, J. E. & Herman, R. K. The molecular identities of the *Caenorhabditis elegans* intraflagellar transport genes *dyf-6*, *daf-10* and *osm-1*. *Genetics* **173,** 1275–1286 (2006).
30. Hou, Y. *et al.* Functional analysis of an individual IFT protein: IFT46 is required for transport of outer dynein arms into flagella. *J. Cell Biol.* **176,** 653–665 (2007).
31. Hurd, D. D., Miller, R. M., Nunez, L. & Portman, D. S. Specific α- and β-tubulin isotypes optimize the functions of sensory cilia in *Caenorhabditis elegans*. *Genetics* **185,** 883–896 (2010).
32. Wright, A. J. & Hunter, C. P. Mutations in a β-tubulin disrupt spindle orientation and microtubule dynamics in the early *Caenorhabditis elegans* embryo. *Mol. Biol. Cell* **14,** 4512–4525 (2003).
33. Lowe, J., Li, H., Downing, K. H. & Nogales, E. Refined structure of αβ-tubulin at 3.5 A resolution. *J. Mol. Biol.* **313,** 1045–1057 (2001).
34. Uchimura, S., Oguchi, Y., Hachikubo, Y., Ishiwata, S. & Muto, E. Key residues on microtubule responsible for activation of kinesin ATPase. *EMBO J.* **29,** 1167–1175 (2010).
35. Efimenko, E. *et al.* Analysis of xbx genes in *C. elegans*. *Development* **132,** 1923–1934 (2005).
36. Schroder, J. M., Schneider, L., Christensen, S. T. & Pedersen, L. B. EB1 is required for primary cilia assembly in fibroblasts. *Curr. Biol.* **17,** 1134–1139 (2007).
37. Yu, S., Avery, L., Baude, E. & Garbers, D. L. Guanylyl cyclase expression in specific sensory neurons: a new family of chemosensory receptors. *Proc. Natl Acad. Sci. USA* **94,** 3384–3387 (1997).
38. Qin, H. *et al.* Intraflagellar transport is required for the vectorial movement of TRPV channels in the ciliary membrane. *Curr. Biol.* **15,** 1695–1699 (2005).
39. Jaglin, X. H. *et al.* Mutations in the β-tubulin gene TUBB2B result in asymmetrical polymicrogyria. *Nat. Genet.* **41,** 746–752 (2009).
40. Tischfield, M. A. *et al.* Human TUBB3 mutations perturb microtubule dynamics, kinesin interactions, and axon guidance. *Cell* **140,** 74–87 (2010).
41. Nielsen, M. G., Turner, F. R., Hutchens, J. A. & Raff, E. C. Axoneme-specific β-tubulin specialization: a conserved C-terminal motif specifies the central pair. *Curr. Biol.* **11,** 529–533 (2001).
42. Deane, J. A., Cole, D. G., Seeley, E. S., Diener, D. R. & Rosenbaum, J. L. Localization of intraflagellar transport protein IFT52 identifies basal body transitional fibers as the docking site for IFT particles. *Curr. Biol.* **11,** 1586–1590 (2001).

METHODS

Constructs, nematode culture and worm genetics. Worms were cultured using standard methods[43]. The fluorescently labelled markers were introduced into single mutants by genetic crossing. The double mutants comprising *dyf-6, ift-81, ift-74, tba-5 and tbb-4* with *klp-11(tm324)* or *bbs-8(nx77)* were produced using genetic crosses and monitoring of the mutant background, Dyf phenotype or deletion sequence (by PCR). The double-deletion mutant, *tba-5(tm4200);tbb-4(OK1461)*, was facilitated using a *dpy-6* marker linked to *tbb-4*. Rescue of *tba-5(qj14)* was carried out by injection of a TBA-5 construct, which was made by cloning its complementary DNA and upstream 7.4-kb promoter region into pPD95.75. For observation of EBP-2 in dendrites and cilia, a construct of EBP-2::GFP driven by an *osm-6* promoter was introduced into wild-type worms.

Cloning of *qj55, qj23, qj14* and *dyf-12*. Complementation tests between two *dyf* mutants were done by crossing N2 male worms with one *dyf* mutant to generate heterozygous males carrying the mutated gene (heterozygous males were used because most *dyf* worms have a low mating efficiency). These males were then mated with hermaphrodites of the second *dyf* mutant. The crossed progeny were analysed by dye-filling assays to determine whether the two mutants are alleles or not. The SNP mappings were done on the basis of documented SNPs between the N2 and the Hawaiian strains (CB4856; ref. 44). In brief, a double mutant of *qj23* with its linkage marker gene *dpy-8* (the worms are dumpy) was made and allowed to mate with CB4856 to obtain the heterozygote worms. From their progeny, 11 Dpy non-Dyf and 5 Dyf non-Dpy recombinants were selected and analysed by SNP markers. *qj23* was narrowed down to a region containing nine genes. These genes were analysed by sequencing to determine the mutation. The same SNP cloning strategy was applied to *qj14* and *dyf-12*, and *dpy-5* and *dpy-6* were used as their linkage markers.

Dye-filling assay. Worms were washed off the culturing plates with M9 buffer and collected in a 15 ml tube by centrifugation at 1,250*g* for 3 min. The DiI (Molecular Probes, Invitrogen) solution was added to a final concentration of 10 $\mu g\,ml^{-1}$. After incubation for 2–4 h, the stained worms were spun down and washed three times with M9 buffer. The worms were then transferred to 2% agarose pads with a drop of 10 mM NaN_3 and observed under a compound microscope with a ×60 objective. The staining ratio is the number of stained amphids or phasmids divided by the total number of amphids or phasmids.

Electron microscopy. Animals were prepared and sectioned for electron microscopy using standard methods[45]. Imaging was carried out with an FEI Tecnai G2 Spirit BioTwin transmission electron microscope equipped with a Gatan 4K × 4K digital camera.

IFT assay and cilium length measurement. IFT and cilium morphology were assayed as described previously[19,21,46]. The worms were immobilized on a 2% agarose pad by anaesthetizing them in 10 mM levamisole. The images were acquired with an Olympus microscope equipped with a ×100, 1.35 NA objective and an Ultraview spinning disc confocal head. The IFT was recorded at 300 ms per frame at 21 °C for 3 min using a CCD (charge-coupled device) camera (ORCA-ER; Hamamatsu). Acquired images were analysed in MetaMorph (Molecular Devices) to create kymographs and calculate the transport rate. For the transport assay of TBB-4::YFP, OSM-9::GFP and DYF-1::GFP, the recorded movies were processed using the basic filters (Sharpen High and Low pass) before creating kymographs. Cilia lengths were measured on projection images, created in MetaMorph from recorded *z* stacks of the cilia. Shown are projection images edited in Adobe Photoshop 7.0 and assembled in Adobe Illustrator 10. During editing, the brightness and contrast of projection images were slightly adjusted in Photoshop.

Y2H. The yeast strain used in this study was PJ69-4A (genotype: *MAT***a***ura3 his3 leu2 trp1 ade2 gal4 gal80 GAL2-ADE2 met2::GAL7-lacZ*). The yeast two-hybrid plasmids were pGAD-C1 and pGBD-C1, containing GAL4 AD (activation domain) and GAL4 BD (DNA binding domain), respectively[47]. The *ift-81* gene was cloned from cDNA of *C. elegans*, and the *ift-74, osm-3, and dyf-6* genes were cloned from their expressed sequence tag (EST) clones. To eliminate self-activation of the expression of the histidine (His) reporter, the genes cloned in pGAD-C1 were co-transformed with empty pGBD-C1 and genes cloned in pGBD-C1 were co-transformed with empty pGAD-C1. Combinations of pGAD-C1 and pGBD-C1 plasmids each carrying one gene to be tested were co-transformed into yeast strain PJ69-4A. Six transformant colonies from each selective plate were streaked onto Leu-, Trp- and His-lacking selective plates to detect the activation of the His reporter. In each set of experiments, both positive and negative controls were included.

Bioinformatics analysis. The domain analyses of DYF-6 and IFT-81 were carried out using SMART (http://smart.embl-heidelberg.de/smart/set_mode.cgi?NORMAL=1) and Coils (for example, ref. 48). TBA-5 or TBB-4 and their orthologues were aligned with Clustal X2 (ref. 49). The heterodimeric structure of TBA-5 and TBB-4 was predicted with Modller9v6 using the porcine brain tubulin heterodimer structure, 1JFF (ref. 33) as a template. The predicted structure was visualized with PyMOL 0.99 (http://www.pymol.org/).

FRAP. FRAP experiments were carried out on a laser-scanning Olympus confocal microscope (FV1000) with a 60 × 1.40 NA objective at 23 °C, and images were acquired using the Fluoview software (version 1.5; Olympus). A 405 nm laser at 40% power was used for photobleaching and images were acquired with a 514 nm laser every 3 or 5 s. The data were normalized to the fluorescence before the bleach. The recovery curve was fitted with an exponential equation $F(t) = F_0 + (F_{\inf} - F_0)(1 - e^{-kt})$, where $F(t)$ is the total fluorescence at time t after the bleach, and k is a constant describing the rate of recovery. F_0 is the fluorescence immediately after the bleach and F_{inf} is the maximum recovered fluorescence. The recovery half-time was calculated by $t_{1/2} = \ln 2/k$ and the percentage of fluorescence recovery was given by $(F_{\inf} - F_0)/(F_{\mathrm{pre}} - F_0)$ (ref. 50), where F_{pre} is the fluorescence intensity before the bleach. It is difficult to determine the exact area of recovery directly, so we used line scans along the cilia to determine the maximum recovered intensity, F_{inf}, in the equation above.

Estimating the diffusion coefficient of GFP in the cilium. Worms expressing free GFP were photobleached and fluorescence profiles along the ciliary length were obtained before and after the bleach. The postbleach fluorescence profiles were subtracted from the prebleach profile. The difference profiles obtained were then fitted to a Gaussian curve. Diffusion coefficients were obtained from these plots, by fitting the normalized bleach depth over time as described in ref. 51. We estimate a value of ~1–5 $\mu m^2\,s^{-1}$ for GFP.

Modelling. See 'Supplementary Information: Modelling'. The modelling codes will be made available on request.

Primers used for cloning the genes and identifying the mutants. For *tba-5*: pKP1056F, 5′-CCTCGGAGGAATTTCAAACG-3′; pKP1056R, 5′-AGCTCCGTAAAGCAGCTTC-3′; pKP1057F, 5′-ATCATTCTCCAGGCCACGTTAC-3′; pKP1057R, 5′-CTGAACTAGTCGAACAAACCCC-3′; pKP1082F, 5′-AATGAGATGCAAGACCGGGACC-3′; pKP1082R, 5′-CTTTCCCACGACCTTTCTTGC-3′; pKP1114F, 5′-AGATTGAGGCTGAAATATGGTG-3′; pKP1114R, 5′-GTCGAGCAGCACCAGTTATTG-3′; pKP1058F, 5′-CCAGTGTCCCGATAGAAAAC-3′; pKP1058R, 5′-GAATCACCGCCAACATGAGA-3′; pKP1059F, 5′-CATCTGGGACGTTCTTTCAC-3′; pKP1059R, 5′-TTCAGGCTCCACTTTATGCC-3′; pKP1117F, 5′-CGAATCCATATCGATGCGAC-3′; pKP1117R, 5′-ACATCTCTGCGTGGCTCTTC-3′; pKP1119F, 5′-TCAAATTTGGCACGTCATCAG-3′; pKP1119R, 5′-CTCCATTTTGGAACTCCCAG-3′; CE1-153F, 5′-CCGTGAAGCAAGTTCAAATGC-3′; CE1-153R, 5′-CTTAACAAGAATTGGTGACCAAC-3′; CE1-170F, 5′-CATGTCCGGCGAATGGATTC-3′; CE1-170R, 5′-AGCCATGGAATCAGCTGTGG-3′; F10D11.2F, 5′-CGCAGATTTGATGACTCCAC-3′; F10D11.2R, 5′-TGGGAACTGGATAAACTGGC-3′; uCE1-969F, 5′-ATACAGTCTAGTGGGGATTGC-3′; uCE1-969R, 5′-CTCAGTGTTACTTGCAGCGG-3′; F02E9F, 5′-AGAGAAGCTTATGCGGTTCG-3′; F02E9R, 5′-AGTGCCGATTTACGATCTCG-3′; F16D3.1-1, 5′-CTATGTACCTTCAAACCTG-3′; F16D3.1-2, 5′-AAACTTGGCACTCCGTGTAC-3′; F16D3.1-3, 5′-AAACTTGGCACTCCGTGTAC-3′; F16D3.1-4, 5′-GTTGGACTTCTGACACCTAG-3′; F16D3.1-5, 5′-CAGCAATGGTAGAGCCATAC-3′; F16D3.1-6, 5′-TGTTCTAAGCCTATCTTGACC-3′; F16D3.1-7, 5′-GCAATTTCGCTTGTTCTAACG-3′; F16D3.1-8, 5′-TCCAAATGAACCCTTGTGCC-3′; F16D3.1-9F(PstI), 5′-AAAActgcagGAGCATGAAGTAGTGTCCTTG-3′; F16D3.1-10R(BamHI), 5′-CACGGGATCCCATTTTTCCATTTGGAGCCATGG-3′; F16D3.1-11F(SalI), 5′-AAAAgtcgacggatccATGCGTGAAATAGTTTCGATTC-3′; F16D3.1-12R(BamHI), 5′-CACGggatccTTTTCCATTTGGAGCCATGG-3′; F16D3.1-12R(XmaI), 5′-CCTACCCGGGGATATTCTTCATCATTTGGATCGA-3′; F16D3.1-13F(SphI), 5′-GAAAGACCTCGCATGCAAATTTA-3′; F16D3.1-14R(BglII), 5′-CCTAagatctCTAATATTCTTCATCATTTGGATCGA-3′; F16D3.1-14R(SphI), 5′-TAAATTTGCATGCGAGGTCTTTC-3′; F16D3.1-15F, 5′-CGGAAATGtCTGTTGGGAACTG-3′; F16D3.1-16R, 5′-CAGTTCCCAACAGACATTTCCG-3′; F16D3.1-17F, 5′-TATCAACCACtGACTGTTGTT-3′; F16D3.1-18R, 5′-AACAACAGTCAGTGGTTGATA. For *tbb-4*: pKP6127F, 5′-TTGGATCTCCGTAGACGTCAC-3′; pKP6127R, 5′-GTCTTCATTGTGATGTGGC-3′; pKP6112F, 5′-GCGTGAGGGCAACTTTTTTG-3′; pKP6112R, 5′-TAGGGATTCTCGCGTCATTG-3′; pKP6135F, 5′-TCTTTGCTTGTGAGCCAATTGG-3′; pKP6135R, 5′-CGGCACGTGTTTTCAAAATAAC-3′; uCE6-1111F, 5′-TCTACATGACCTACATGTCTG-3′; uCE6-1111R, 5′-TGGACATTTACACAGAACCTG-3′; pas23221F, 5′-GTCGAGAAGTTATGTGTGCAG-3′; pas23221R, 5′-AAGATGTCCATCTATGGACCG-3′; uCE6-1120F, 5′-CAACCACATCGGATATGGTAG-3′; uCE6-1120R, 5′-CGTTGGCTTTGACGTACGTTC-3′; tbb4-1F, 5′-GCCATTTAAGGACACACCTCC-3′; tbb4-2R, 5′-CACGCGTAAGGCGTTGAACC-3′; tbb4-3F, 5′-CGGAAATTGAGCGACATCTCC-3′; tbb4-4R, 5′-GCCATCATATTCTTGGCGTCG-3′; tbb4-5F, 5′-TCCAGAGGAAGCCAGCAATAC-3′; tbb4-6R, 5′-CTATGCATTTGTAGT-

DOI: 10.1038/ncb2268

AATGTATTACTG. For *ift-81*: pKP6103F, 5′-TGTCTAGTTCAAAAGCCCGG-3′; pKP6103R, 5′-TTGTAGCAGATCCTACCCTACC-3′; pKP6104F, 5′-TCCAA-TGTTACGCTACCAGC-3′; pKP6104R, 5′-TGACAAGGCAACCACCATTG-3′; pKP6120F, 5′-GATTCAGATCAAACAGAGGTGG-3′; pKP6120R, 5′-TCGTGGC-ACCATAAAAGTG-3′; pKP6151F, 5′-AGCAATTATAGTGTCATTGCCG-3′; pKP6151R, 5′-TTAAAAGCTGGCTCTAGTGTTG-3′; pKP6150F, 5′-AATCGTCC-TAGTTATCCACGG-3′; pKP6150R, 5′-TGGGGGTGAAAGAGATATGTC-3′; uCE6-907F, 5′-GCAGACATGGGAAGAAGATG-3′; uCE6-907R, 5′-GTGA-CGCATGAATGGCTGG-3′; uCE6-929F, 5′-CGATGGAATTGAGTACTTCGATG-3′; uCE6-929R, 5′-GTACATTTACTTACCTCCCACAC-3′; pas16937F, 5′-AACGT-GGTGAGAACGTGATG-3′; pas16937R, 5′-GTACTGAACTCATCTCTGCC-3′; Y34B4A-F, 5′-CTCAGATTCAGCTGTACCTC-3′; Y34B4A-R, 5′-TCATTCCATTC-TGCCGAAGG-3′; pas16936F, 5′-ATCTAATTGTCTCGAGTGCG-3′; pas16936R, 5′-GTCTCGCTCATTGAAATCTG-3′; IFT-81-1F, 5′-ATAGCAAAGAGCCCAGCA-AC-3′; IFT-81-2R, 5′-CGCACATTGTAACTTTGTGCC-3′; IFT-81-3F, 5′-TATCA-GCAGGTCCACTTGGG-3′; IFT-81-4R, 5′-CTAACACGATGAATTCAGATAGC-3′; IFT-81-5F, 5′-AAGTAAGGGAGTTCTTTAGCG-3′; IFT-81-6R, 5′-CTGTCGGC-TGCACATTTATC-3′; IFT-81-7F, 5′-AATGGCTTCAGACGTCAGAG-3′; IFT-81-8R, 5′-ACGCAGATTGTGTCTCTTAGC-3′; IFT-81-9F, 5′-AAGCAAAACCAGGT-GATGAAC-3′; IFT-81-10R, 5′-GTTAGCAGAGGTATCTGATAC-3′; IFT-81-11F, 5′-TGCGTTCCCGATTTTGCAAG-3′; IFT-81-12R, 5′-TGAAATGTCACTC-TGCAACTG. For *dyf-6*: Dyf-6-1F, 5′-CTCAATGACCTAATATGCTC-3′; Dyf-6-2R, 5′-AGAATGTCAGAAACGTCTGC-3′; Dyf-6-3F, 5′-TTTGAATCC-GTTTCTTCGGG-3′; Dyf-6-4R, 5′-GTCActgcagCAGGTGACTCTATTCATT-GAAGC-3′; Dyf-6-5F, 5′-CTAGcccgggAAGTTCCAATCTGTCCATTGTTTC-3′; Dyf-6-6R, 5′-CAGTCCCGGGCTCGCATGCGAGCTCCATTGGATTTTCCAAT-GCCTG-3′; Dyf-6-7F, 5′-TTAAgagctcATGGCGGCAAACGGAGAGT-3′; Dyf-6-8R(XmaI), 5′-CTAGCCCGGGAAAGTTCCAATCTGTCCATTGTTTC-3′; Dyf-6-9F, 5′-CGTTGAATCCGACAGATACC-3′.

43. Brenner, S. The genetics of *Caenorhabditis elegans*. *Genetics* **77,** 71–94 (1974).
44. Wicks, S. R., Yeh, R. T., Gish, W. R., Waterston, R. H. & Plasterk, R. H. Rapid gene mapping in *Caenorhabditis elegans* using a high density polymorphism map. *Nat. Genet.* **28,** 160–164 (2001).
45. Yoshimura, S., Murray, J. I., Lu, Y., Waterston, R. H. & Shaham, S. *mls-2* and *vab-3* control glia development, hlh-17/Olig expression and glia-dependent neurite extension in *C. elegans*. *Development* **135,** 2263–2275 (2008).
46. Hao, L., Acar, S., Evans, J., Ou, G. & Scholey, J. M. Analysis of intraflagellar transport in *C. elegans* sensory cilia. *Methods Cell Biol.* **93,** 235–266 (2009).
47. James, P., Halladay, J. & Craig, E. A. Genomic libraries and a host strain designed for highly efficient two-hybrid selection in yeast. *Genetics* **144,** 1425–1436 (1996).
48. Signor, D., Wedaman, K. P., Rose, L. S. & Scholey, J. M. Two heteromeric kinesin complexes in chemosensory neurons and sensory cilia of *Caenorhabditis elegans*. *Mol. Biol. Cell* **10,** 345–360 (1999).
49. Larkin, M. A. *et al.* Clustal W and Clustal X version 2.0. *Bioinformatics* **23,** 2947–2948 (2007).
50. Cheerambathur, D. K., Brust-Mascher, I., Civelekoglu-Scholey, G. & Scholey, J. M. Dynamic partitioning of mitotic kinesin-5 cross-linkers between microtubule-bound and freely diffusing states. *J. Cell Biol.* **182,** 429–436 (2008).
51. Mullineaux, C. W., Nenninger, A., Ray, N. & Robinson, C. Diffusion of green fluorescent protein in three cell environments in *Escherichia coli*. *J. Bacteriol.* **188,** 3442–3448 (2006).

nature cell biology

DOI: 10.1038/ncb2268

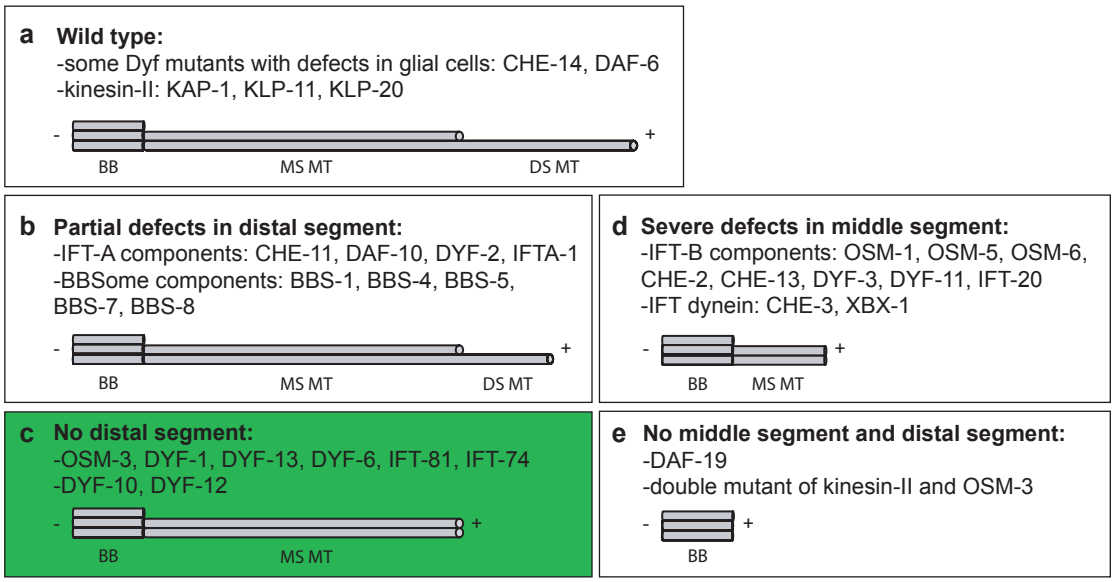

Figure S1 Classes of mutations that cause truncations of cilia and ciliary morphology of four putative distal segment defective *dyf* mutants. (**a**) The wild type axoneme is tripartite consisting of a modified basal body (BB) or transition zone (TZ), made of nine MT triplets a middle segment (MS) of nine doublet MTs and nine distal singlet MTs (DS) that are extensions of the A tubules of the doublets (only one of each of the nine MT structures is shown). The kinesin-II motor mutants and the *dyf* mutants affecting glial cells have intact axonemes. (**b**) Mutations in IFT-A subunits and in BBSome components cause partial truncations of the distal singlets. (**c**) Mutations in *osm-3* and those discussed in the current manuscript specifically result in loss of the distal segments. (**d**) Mutations in some IFT-B components and IFT dynein cause complete loss of the distal segment and partial loss of the middle segment. (**e**) Mutation of DAF-19, an RFX transcription factor, and the double mutant of kinesin-II and OSM-3 lead to complete loss of cilia.

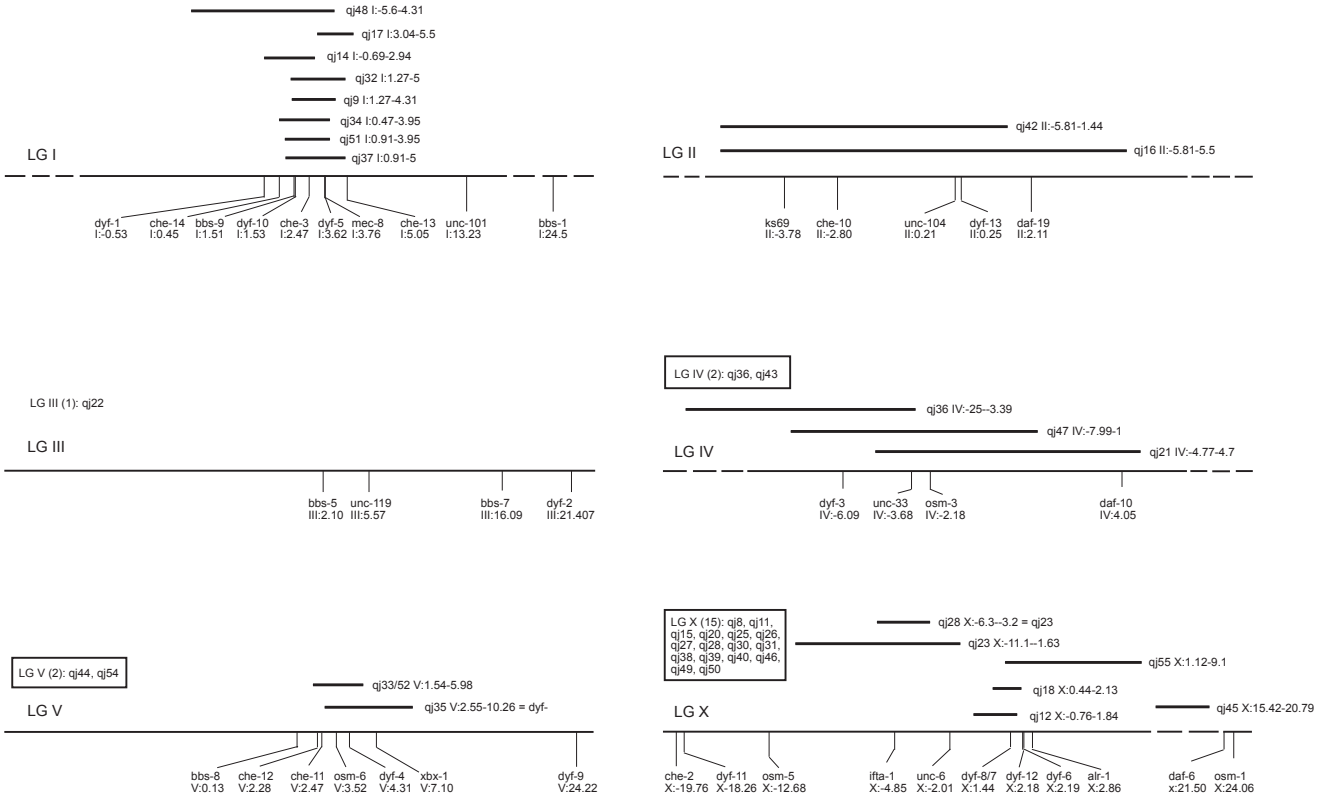

Figure S2 Genetic linkage of the *dyf* mutants. The six chromosomes are represented by six solid or broken lines. The known *dyf* mutants are shown below each of the six chromosomes based on their positions. The newly isolated *dyf* mutants are drawn above the chromosome based on their mapped loci. Those that were not mapped to a specific locus are placed in a square.

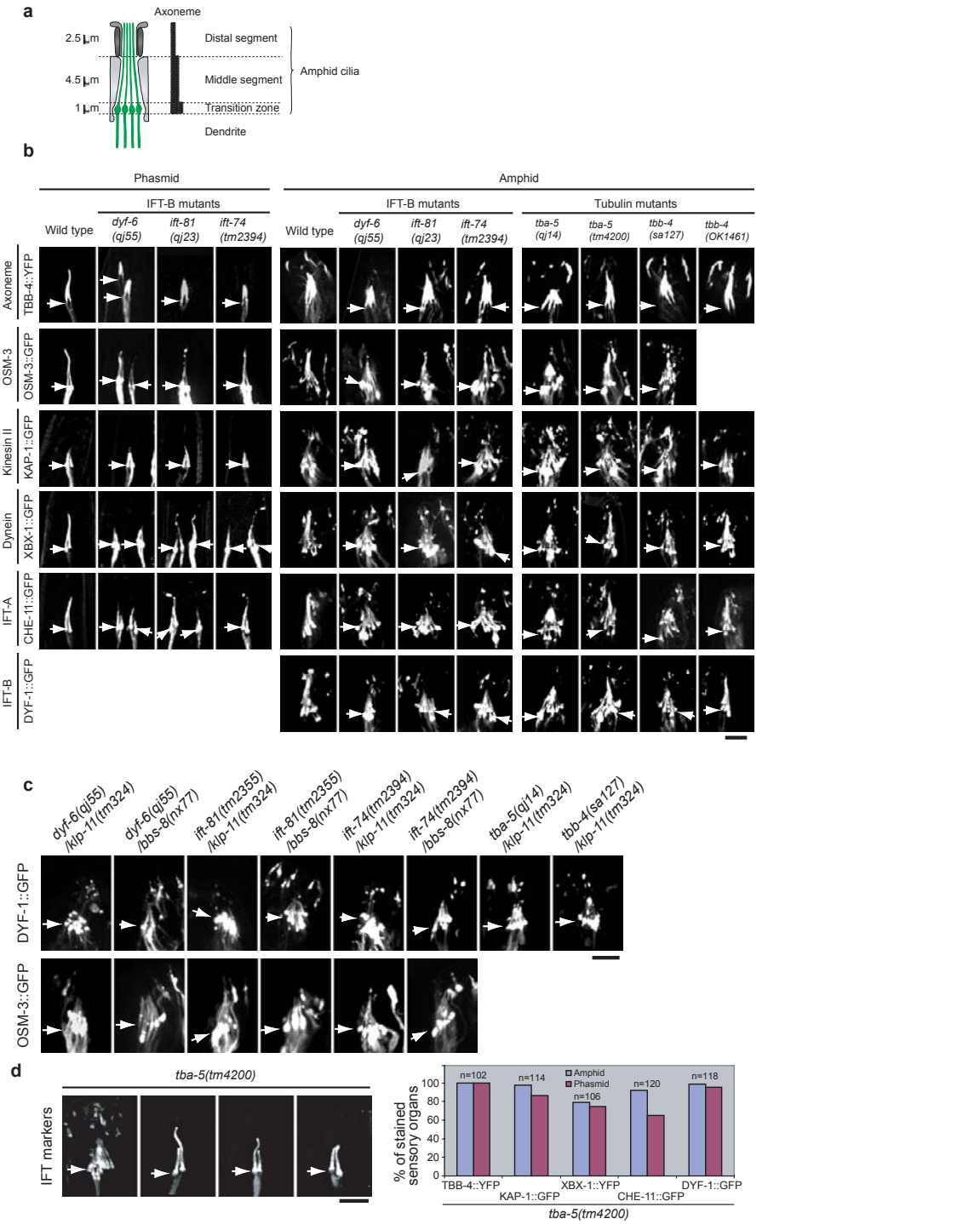

Figure S3 Characterization of the *dyf-6*, *ift-81*, *ift-74, tba-5 and tbb-4* mutants. (**a**) Cartoon of the amphid ending. (**b**) Tubulin (TBB-4::YFP), IFT motors (OSM-3::GFP, KAP-1::GFP; XBX-1::GFP), and IFT particle subcomplex A and B markers (DYF-1::GFP, CHE-11::GFP) were used to visualize the morphology of the sensory neuronal cilia in the phasmid and amphid. (**c**) The DYF-1::GFP marker was used to visualize the amphid ciliary morphology of the double mutants, *dyf-6;klp-11*, *ift-81;klp-11* and *ift-74;klp-11*, *tba-5/klp-11, tbb-4/klp-11*, demonstrating that *dyf-6*, *ift-81* and *ift-74* are distinct from *tba-5(qj14)* and *tbb-4(tm324).* The OSM-3::GFP and DYF-1::GFP markers were used to compare the ciliary morphology in *dyf-6*;*klp-11*, *ift-81*;*klp-11* and *ift-74*;*klp-11 and in dyf-6;bbs-8*, *ift-81;bbs-8* and *ift-74;bbs-8,* demonstrating that the overexpression of OSM-3::GFP was able to rescue the ciliary length in *dyf-6, ift-81 and ift-74*. (d) Secondary effects of IFT markers in the *tba-5(tm4200)* deletion mutant. In rare cases, IFT markers cause ciliary defects in *tba-5(tm4200)* (left panel); such an effect is substantiated and quantified by DYF assays. Variable percentage of the *tba-5(tm4200)* worms are not stained when containing KAP-1::GFP, XBX-1::YFP, CHE-11::GFP and DYF-1::GFP. In comparison, all the *tba-5(tm4200)* worms containing TBB-4::YFP are stained (right panel). n indicates the number of amphids or phasmids. Arrows point to transition zones with cilia oriented upward. In (b-d), Bar=5 µm.

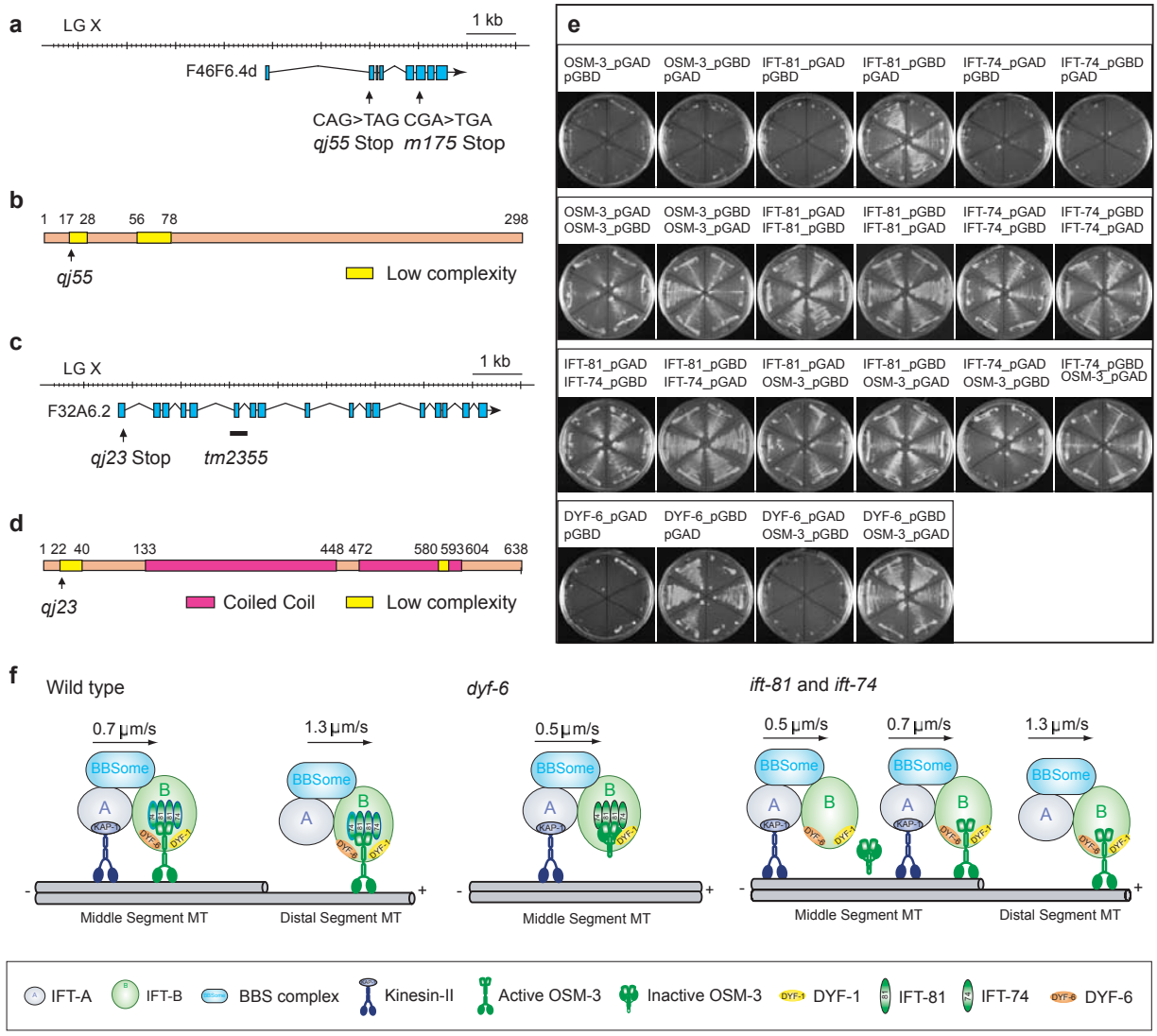

Figure S4 Three IFT-B components regulate OSM-3 activity. (**a**) Schematic of one of the *dyf-6* splice variants, F46F6.4d. *qj55* and a known mutant m175, both contain a point mutation that introduces a stop codon. (**b**) Structure of the gene product of *dyf-6* (F46F6.4d) deduced using the SMART program reveals only two low complexity regions. (**c**) Schematic of the *ift-81* (F32A6.2) gene. *qj23* contains a point mutation that introduces a stop codon into the end of the first exon. (**d**) Analysis of IFT-81 using the program COILS predicts two coiled-coil domains. (**e**) Yeast 2 hybrid test of interactions between OSM-3 and IFT-81, IFT-74 and DYF-6. The gene constructs were firstly tested with the vector pGBD or pGAD as negative control. Two of them (IFT-81-pGBD and DYF-6-pGBD) activated yeast growth and were not considered further. The known interactions between OSM-3 and OSM-3, IFT-81 and IFT-81, IFT-81 and IFT-74 were used as positive controls. This indicated that IFT-81 and IFT-74, but not DYF-6 could interact with OSM-3. (**f**) Models to explain the function of IFT-81, IFT-74 and DYF-6. In wild type worms, IFT-81 and IFT-74 can interact with OSM-3 and DYF-6 plays a role in maintaining the active conformation of OSM-3. In the *dyf-6* mutant, OSM-3 is attached to the IFT machinery in the inactive conformation and is moved by kinesin-II. In the *ift-81* or *ift-74* mutants, the OSM-3 motors are mainly detached from the IFT machinery but they can interact weakly with other IFT components allowing over-expressed OSM-3::GFP to contribute to IFT and partially rescue cilium length in some mutant backgrounds (Figure S3c, Tables S3 and S4).

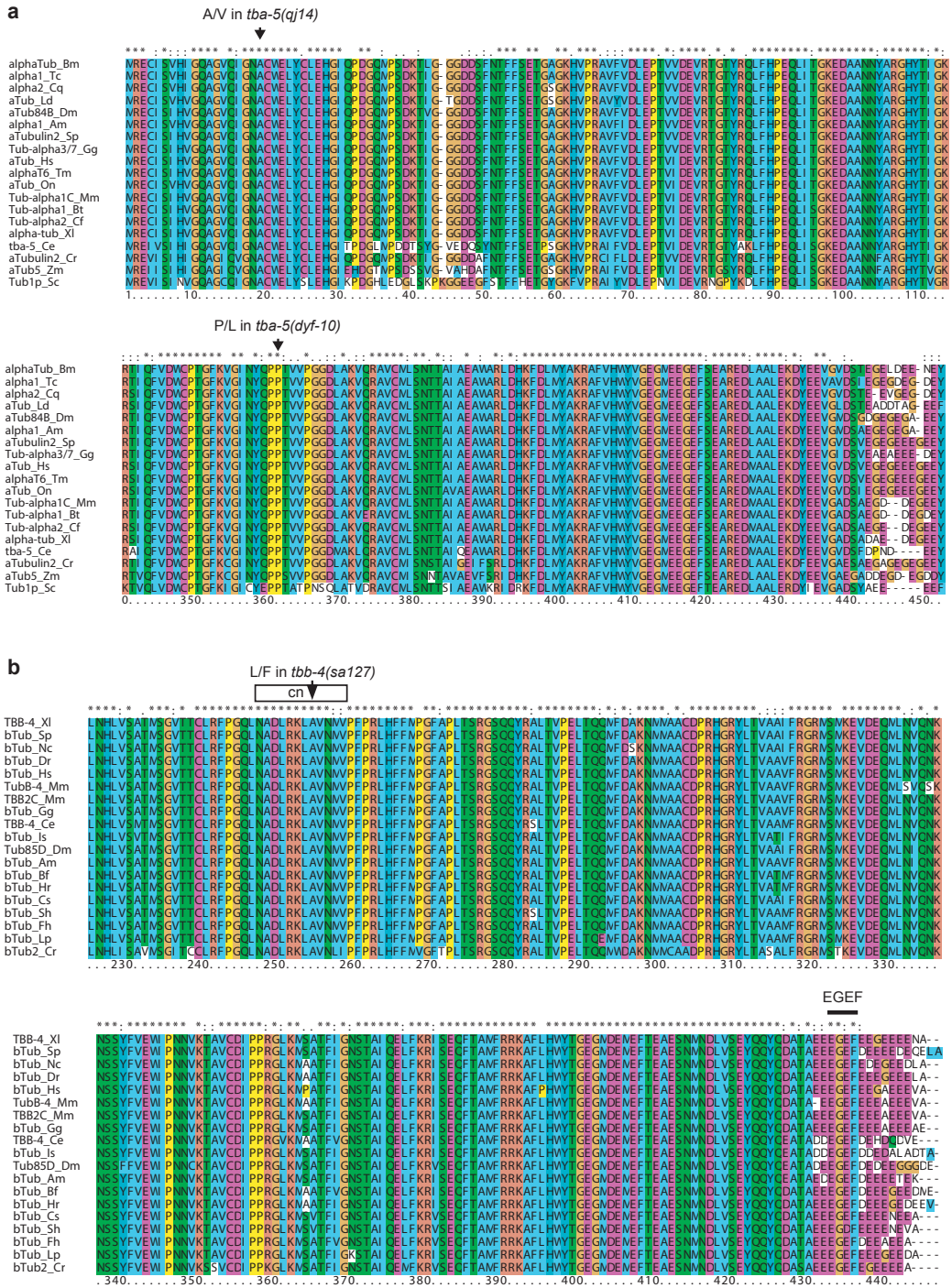

Figure S5 Multiple alignments of TBA-5 or TBB-4 and their orthologs from different organisms. (**a**) Ala19 and P361 (P360 in TBA-5_Ce) in TBA-5 are highly conserved across species, and they are converted to Val in *tba-5(qj14)* and Leu in *tba-5(dyf-10)*. (**b**) Leu253 in TBB-4 is highly conserved across species, and it is converted to Phe in *tbb-4(sa127)*. The box indicates one of the colchicine (cn)-binding motifs and the arrows point toward the mutation site. At the tail region, a small motif (EGEF) which is known to be motile cilia-specific, is highly conserved in the ciliated organisms, including *C. elegans*. The species abbreviations are: *Am, Apis mellifera (honey bee); Bf, Branchiostoma floridae; Bm, Bombyx mori; Bt, Bos Taurus; Ce, Caenorhabditis elegans; Cf, Canis familiaris; Cq, Culex quinquefasciatus; Cr, Chlamydomonas reinhardtii; Cs, Clonorchis sinensis; Dm, Drosophila melanogaster; Dr, Danio rerio; Gg, Gallus gallus; Fh, Fasciola hepatica; Hr, Halocynthia roretzi; Hs, Homo sapiens; Is, Ixodes scapularis; Ld, Lepidoglyphus destructor; Lp, Loligo pealei; Mm, Mus musculus; Nc, Notothenia coriiceps; On, Oncorhynchus nerka; Sc, Saccharomyces cerevisiae; Sh, Schistosoma haematobium; Sp, Strongylocentrotus purpuratus; Tc, Tribolium castaneum; Tm, Torpedo marmorata; Xl, Xenopus laevis; Zm, Zea mays.*

Supplemental Material: Modeling

Our model tests whether; (i) the delivery of tubulin by IFT can maintain a cilium at its observed steady state length while its axonemal MT tips undergo dynamic instability; and (ii) this mechanism can account for the axoneme dynamics revealed by our FRAP curves i.e. the form (e.g. single or double exponential), half-time and extent of recovery. The framework of our model, namely the IFT-dependent delivery of tubulin subunits, is based on the balance point model. However, we have significantly extended this deterministic model to produce an agent-based, stochastic model that includes: (i) the dynamic instability of MT plus ends; and (ii) the loading of IFT particles containing a number of tubulin subunits, randomly chosen between zero and a pre-determined maximum, at the base of the cilium. The model assumptions are the simplest ones compatible with the available FRAP data and its results suggest that delivery of tubulin by IFT provides an efficient mechanism for maintaining the axonemal MT tips in close axial proximity while they undergo dynamic instability, as observed experimentally. Naturally the model results do not exclude contributions from unknown factors that we did not test.

MT Dynamic Instability

MT plus ends exhibit dynamic instability (DI) characterized by stochastic switches between phases of growth and shrinkage, termed catastrophe (from growth to shrinkage) or rescue (from rescue to shrinkage). For any chosen set of DI parameters i.e. growth and shortening velocities, v_g and v_s, rescue and catastrophe frequencies, f_{res} and f_{cat}, the average velocity at which a MT population grows (J) is given by $J = \frac{v_g f_{res} - v_s f_{cat}}{f_{res} + f_{cat}}$ [1].

When $J > 0$ (the unbounded growth regime), MTs exhibit growth on average, whereas

when $J < 0$ (bounded regime), MTs tend to disassemble all the way back to their nucleation site. During one DI cycle, the characteristic lengths by which the MTs grow and shrink are $l_{grow} = v_g / f_{cat}$ and $l_{short} = v_s / f_{res}$, respectively. It is worth emphasizing that the DI parameters of individual MT plus ends in the cilium cannot be measured directly using currently available imaging techniques; however, estimates can be made based on experimental data (see below).

In the cilium, MTs are arranged with parallel polarity patterns, having their minus ends at the transition zone (TZ) and their plus ends facing the tip of the cilium. In previous EM studies[2] the relative positions of the tips of the 9 MS and DS MTs were found to be axially constrained to a submicron region. Similarly in our FRAP experiments, the observed fluorescence recovery region is less than a micron wide axially, coincident with the position of the MS and DS tips. This provides an upper limit for the DI parameters, $l_{grow} = v_g / f_{cat}$ and $l_{short} = v_s / f_{res}$ associated with MT plus ends at the tips of the MS and DS. However, for a population of MTs such as those in the cilium undergoing DI at fixed rates (i.e. v_g , v_s, f_{res} and f_{cat} = constant), the variance in MT length distribution (i.e. the variance of the MT tip positions) is expected to increase with time, unless constrained by specific regulatory mechanisms[8,9]. This raises the question of how the tips are maintained within a submicron region, and could regulation by IFT play a role?

The length of doublet and singlet MTs in the cilium: Balance Point Model and MT DI and turnover by FRAP.

Marshall et al.[3] proposed the following hypothesis; (i) if the rate of polymerization of the MT tips in the cilium is limited by the rate of delivery of tubulin subunits to the tips (i.e $v_g = \gamma L$ where v_g is the rate of polymerization, L is MT length and γ is a proportionality coefficient); and (ii) if there is a constant depolymerization rate (v_s = c, constant); then a steady-state ciliary MT length can be reached and maintained.

The *C. elegans* sensory cilia investigated in our study are ~7-7.5 μm in length, each being composed of 9 doublet MTs which are differentiated longitudinally into two structurally distinct domains; namely (i) a proximal 4-4.5 μm long middle segment (MS) whose nine doublets are composed of 13 (A) +11 (B) protofilament (pf) tubules; and (ii) 13 pf singlet extensions of the middle segment A-tubules that form the axoneme's distal segment (DS) [2] (See Fig. 1A). Experiments in the current study suggest that the tips of the MS and the DS MTs display dynamic instability, and therefore they recover from photobleaching with exponential kinetics. However, as noted above, this recovery is limited to a < 1 μm region of the MS and DS tips, while the remaining portions of the doublet and singlet MTs do not exhibit any detectable recovery.

Here, in a stochastic version of the proposed "Balance Point Model", we first test if the balance between IFT and MT turnover via DI, on its own, can maintain the highly dynamic tips of the MS and DS MTs within the narrow region observed or if other regulatory mechanisms are necessary. We then test if the resulting MT DI parameters, in concert with IFT-based tubulin transport and delivery can account for the axoneme dynamics as revealed by the experimental FRAP recovery curves, by performing

theoretical *In Silico* FRAP experiments. Finally, we ask if the stoichiometry of [tubulin subunits] : [IFT-motor-cargo-complexes] that is suggested by fitting the model to our FRAP results can also account for the observed faint transport of YFP-tubulin in *in vivo* transport assays (under conditions where labeled IFT particle and motor subunits yield robust tracks in equivalent transport assays[4]).

Stochastic IFT-MT Dynamics Model

The model describes the evolution of the positions of pre-assembled, full-length MTs' plus ends facing the tips of the cilium that undergo DI concurrent with the transport of tubulin subunits from the transition zone (TZ) along the length of the MTs to the tips and back by IFT. In the model, we assume that the IFT-dependent transport rates of the tubulin dimers from the TZ to the MT tips occur at the experimentally observed average rates along the MS doublets (0.7 μm s^{-1}), through the cooperation of two types of anterograde kinesin-2 motors (kinesin-II and OSM-3), and along the DS singlets (1.2 μm s^{-1}), by only one type of anterograde kinesin-2 (OSM-3), while dynein is the sole retrograde transport motor. In the model, a MS doublet's length increases/decreases by 8 nm through the addition/dissociation of 11 tubulin subunits i.e. we assume that the tubulin subunits preferentially exchange with the tips of the shortest/longest pfs, so that the pf tips grow/shorten cooperatively as a 'front' rather than individually). Hence the addition or dissociation of a single tubulin subunit increases or decreases the length of a MS MT by 8/11 nm. Similarly, in the model, a DS singlet's length increases or decreases by 8 nm through the addition or dissociation of 13 tubulin subunits, and hence the

addition or dissociation of a single tubulin subunit increases or decreases the length of a DS MT by 8/13 nm.

The stochastic model thus describes the dynamics of the MS and DS MT tips over time, computed with a custom made Matlab/Octave code, run on a personal laptop computer or on a Linux cluster (11-nodes each with a 2 x Opteron-246 processor). In the model, starting with the initial states and positions of the MT tips and the initial assembly-state and position of the IFT-motor-cargo complexes (see Initial Conditions), at each time step, we compute the new states and positions of the MT tips, and the new assembly-state and position of the IFT-motor-cargo complexes for the next time step, according to the rules and/or simplifying assumptions listed below. The model is run typically for 120000 time steps, one computational time step typically corresponding to 0.01 s (the model is non-dimensionalized with τ=0.01 s).

Rules for motor assembly-states, IFT rates, turnaround and tubulin-delivery

1- The total numbers of kinesin-II, OSM-3 and dynein motors are maintained constant and equivalent. This is consistent with the data and conclusions of Pan et al (ref. 5), which suggests that kinesin-II and OSM-3 are present in a 1:1 ratio on IFT particles. The ratio of dynein molecules to other motors is not known, but the simplest assumption is a 1:1:1 ratio, and its function is to drive the retrograde transport of kinesin-2 motors, IFT particles and exchanged tubulin back to the TZ.

2- The IFT-motor-cargo complexes assemble only at the TZ: The two anterograde motors and the sole retrograde motor are combined randomly on the IFT particles as a 3-motor-

complex. In addition, at the TZ, upon assembly of each new IFT-motor-complex, a random number of MS-specific and DS-specific tubulin isotype cargo molecules (i.e. a randomly chosen number between 0 and a pre-determined maximal value specific for each tubulin isotypes) are loaded onto each IFT-motor-complex. For every newly assembled IFT particle complex at the TZ, both types of anterograde motor are bound in an active state and the retrograde motor is bound as inactive cargo.

3- Each IFT-motor-cargo complex assembled at the TZ "hops" onto a randomly chosen MT, and moves along the same MT, both in the anterograde and the retrograde direction, until it returns to the TZ (i.e. the IFT-motor-cargo complexes do not switch between MT tracks). The number of IFT motor/cargo complexes moving on each MT was kept approximately the same, a restriction that was found to be needed to maintain the MT tips within a submicron region.

4- Anterograde IFT occurs at an average rate of 0.7 $\mu m\ s^{-1}$ along the MS doublets, through the cooperation of kinesin-II and OSM-3, and at an average rate of 1.2 $\mu m\ s^{-1}$ along the DS singlets, solely mediated by OSM-3. Retrograde IFT occurs at an average rate of 1.0 $\mu m\ s^{-1}$ along the length of the cilium, solely mediated by dynein.

5- When an IFT-motor-cargo complex reaches the tip of the doublet in the anterograde direction, (i) kinesin-II and a MS-specific tubulin isotype are dissociated from the complex; (ii) the kinesin-II motor waits at the tip of the doublet until it is picked up by a retrograde IFT-motor-cargo complex; (iii) OSM-3 continues along the DS along with the DS-specific tubulin and the remaining IFT-motor-cargo complex components.

6- When an IFT-motor-cargo complex reaches the tip of the singlet in the anterograde direction (i) the DS-specific tubulin isotype is dissociated from the complex; (ii) OSM-3

is inactivated while dynein is activated, hence the IFT-motor-cargo complex turns around; (iii) a number of dissociated tubulin subunits (up to a pre-determined maximal value) are picked up by the dynein-powered retrograde IFT-cargo-complex, to be transported back to the TZ.

7- When an IFT-motor-cargo complex reaches the tip of the doublet in the retrograde direction; (i) kinesin-II motors waiting to be picked up and (ii) dissociated tubulin subunits (up to a pre-determined maximal value) are picked up by the dynein-powered retrograde IFT-cargo-complex, to be transported back to the TZ.

8- When an IFT-motor-cargo complex reaches the TZ in the retrograde direction the complex dissociates and a new IFT-motor-complex is reassembled randomly as described in step (2).

DI of the MT plus-ends

The dynamics of the MT plus ends is computed using a Monte Carlo algorithm, based on the 4 parameters of MT dynamic instability and the built-in random number generator in Matlab/Octave. To summarize, the MT tips are either in a growth or a shrinkage state at all times, and their dynamic properties are fully described by the four parameters of dynamic instability: v_g, v_s (effective growth and shrinkage rates in nm per second, which can be converted into a 'subunits per second' rate by multiplying with 11/8nm and 13/8nm for the MS and the DS MTs, respectively) and f_{cat} and f_{res} (frequency, per second). In each model run, the transition frequencies between the phases of growth and shrinkage and vice-versa for the MS and DS MTs' plus ends (f_{catMS}, f_{catDS} and f_{resMS}, f_{resDS}, respectively), as well as their depolymerization rate (v_{sMS} and v_{sDS}) are fixed (see Table

S5). The polymerization/growth rate of the MS and DS MTs' plus ends is limited by a prescribed rate (v_{gMS} and v_{gDS}), but the effective polymerization rate (v_{effMS} and v_{effDS}) depends on the amount of available free tubulin subunits present as a result of delivery by IFT at the tip of each MT at a given time step when that MT tip is in a growth state. At each time step, t_n, for each MT plus end undergoing growth (or shrinkage) in the previous time step, t_{n-1}, a catastrophe (or rescue) event occurs if a random number r, Matlab/Octave function *rand*, satisfies $r < P_{cat} = 1- \exp(-f_{cat}\,\Delta t)$ (or if $r < P_{res} = 1- \exp(-f_{res}\,\Delta t)$) where Δt is the simulation time step. Once the state of each MS/DS MT tip is determined for the new time step t_n, the change in MT length is calculated based on a constant shrinkage rate or its current effective growth rate as follows. For a MT plus end in the growth state, the effective polymerization length of the MT at time t_n, ($v_{eff}(t_n)\,\Delta t$) is determined as the minimum between $v_g\Delta t$ (in nm) and the polymer length corresponding to the available free (GTP) tubulin subunits at the MT tip (converted to nm by multiplying with 8nm/11 or 8nm/13 for the MS or the DS, respectively). The effective growth rate v_{eff} is thus equal to the effective polymerization length divided by Δt. For a depolymerizing MT the shrinkage length is $v_s\Delta t$. Once these lengths are determined, the new positions of the (MS and DS) MT tips are computed and updated as $pos(t_n) = pos(t_{n-1}) + \Delta x$, where $\Delta x = - v_s\,\Delta t$ for a depolymerizing MT, and $\Delta x = v_{eff}\,\Delta t$ for a polymerizing MT. If a DS MT depolymerizes down to the plus tip of its MS, the DS plus end is immediately switched to rescue (the singlet MTs are not allowed to depolymerize below their associated doublet's length).

Initial Conditions

Initially, the plus ends of all 9 doublets and singlets are positioned at 4.5 and 7 μms from the TZ, respectively, and the MT tips are randomly chosen to be either in a growth or shrinkage state with probability 0.5. We chose to start the computation at the normal adult cilium length since we are primarily interested in the *maintenance* of ciliary length, not the initial establishment of the cilium. All our experiments were performed on adult worms with pre-assembled cilia, and it is possible that the *de novo* assembly of cilia utilizes additional mechanisms and factors.

At the initial time step, IFT-motor-cargo-complexes are randomly assembled in either 3-motor (kinesin-II/OSM-3/dynein) or 2 motor (OSM-3/dynein) complexes. Initially, all IFT-motor-cargo-complexes are assumed to be active in the anterograde direction: both the kinesin-II and OSM-3 motors are assumed to be active in all 3-motor (kinesin-II, OSM-3, dynein) IFT-motor-cargo complexes, and OSM-3 is assumed to be active in all 2-motor (OSM-3, dynein) IFT-motor-cargo complexes. IFT-motor-cargo-complexes are equivalently distributed among the 9 ciliary MTs. In addition, the initial position of each 3-motor (kinesin-II, OSM-3, dynein) and 2-motor (OSM-3, dynein) IFT-motor-cargo complex is chosen randomly along the MS and the DS of the MT, respectively. The model is run for at least 40000 time steps to equilibrate the IFT distribution along the length of the MTs before analyzing the distribution of the tips or simulating FRAP. The distribution of tips and FRAP recovery are run for at least 60000 time steps after equilibration.

In Silico Tubulin FRAP

To simulate our FRAP experiments, we first calculate the total pre-bleach fluorescence intensity in a pre-determined bleach region (e.g. a region from the TZ to the tips of the

cilium or a small region covering the presumptive position of the MS and DS tips). To do this, we calculate; (i) the length of the MT segments in the region, L_{MS} and L_{DS}, and based on these lengths, (ii) the total number of tubulin subunits in polymerized form (which is $L_{MS}*11/8 + L_{DS}*8/13$) (iii) the number of fluorescent tubulin subunits in transit in the anterograde and retrograde direction, and if applicable, (iv) the number of delivered tubulin subunits at the tips of the MS or DS. At the time of the bleach, all the subunits (in polymerized form, in transit or delivered to the tips) within the bleach region are assumed to lose fluorescence and the total fluorescence intensity is set to zero, portraying a complete bleach. The locations of the bleached MT portions' ends, the bleached tubulin subunits in transit (both in anterograde and retrograde direction) and the bleached deposited subunits at the MS and/or DS tips are stored to be followed in subsequent time steps,. At each subsequent time step, both the bleached and fluorescent portions of the MT lattice (i.e. the total number of bleached and fluorescent tubulin subunits in polymerized form), the bleached and fluorescent tubulin subunits in transit in the anterograde/retrograde direction and the bleached and fluorescent subunits deposited within the FRAP monitored region are computed through dynamic instability, transport and delivery. The total fluorescent tubulin subunit number within the monitored region is stored in the fluorescence intensity array. Once the fluorescence intensity values are stored for all time points, the intensity is summed over 100 steps (equivalent to 1 s in real time) and sampled every 3 s to mimic the experimental data. Finally, the values are normalized to the pre-bleach intensity and white noise is added using the *randn* function in Matlab with mean and variance based on measured normalized values from experimental data in a 5x5 pixel dark region following photobleaching to estimate the

background fluorescence and the standard deviation. The results are plotted over time, and fit by a single exponential curve to calculate the $t_{1/2}$ and the percent recovery.

Modeling transport at low or high IFT rates

We did not exhaustively search the parameter space beyond that indicated in Table S5, but we did explore the range of IFT velocities that is compatible with the experimentally-observed tip excursion and FRAP data. Specifically, when we reduced the velocity of OSM-3 so that it became the same as kinesin-II, i.e. IFT particles moved at 0.5 μm s^{-1} all along the cilium, leaving all other parameters the same, then steady state cilium length was not maintained as all the axonemal MTs persistently shortened. Increasing the number of motors by 20% rescued the length of the axonemal MTs, but *In Silico* FRAP of such a cilium exhibited little recovery in the MS. In contrast, when we increased kinesin-II's velocity to 1.3 μm s^{-1} like OSM-3, the MTs equilibrated to a new steady state length or kept growing persistently at a slow rate, but displayed *In Silico* FRAP recovery curves that were different from our *in vivo* FRAP data, particularly in the middle segment, where recovery was very slow and less than 15%. These model results make several predictions concerning the relationship between the number, speed and types of kinesin-2 motors driving IFT and the steady state length, stability and dynamic properties of axonemal MTs that can be tested in the future using FRAP and modeling of various types of wild type and mutant cilia that differ in their length, dynamics and form of motor cooperation.

Table S5. Model Parameters. *Justification:* Pan et al.[5] showed that kinesin-II and osm-3 are present in a 1:1 ratio, and we assume that dynein is also present in a 1:1 ratio with these motors. If there were more dynein, the model would still work, as dynein's role is simply to return motors and subunits. A much smaller number of dynein molecules could be a problem, unless they could carry many motors back. We tried different numbers of tubulin subunits carried per motor, in the range of 1-15, the numbers in parentheses worked well - the important result is that OSM-3 has to carry more tubulin subunits than kinesin-2 to maintain the length of the DS tips within a submicron range. The number of tubulin subunits is coupled with the number of IFT complexes; a higher number of IFT complexes necessitates a lower number of tubulin subunits, or vice versa. 500 complexes with 2 tubulin subunits on kinesin-2 and 3 on OSM-3 gave the best results, but our search was not exhaustive. A few hundred IFT complexes is consistent with EM tomographs on *Chlamydomonas*[6] assuming similar IFT train and particle sizes. Parameters were varied, parameters in parenthesis are the ones used in Fig. 5d. Note that the growth rates v_{gMS} and v_{gDS} (the maximal rates, not the effective rates which are determined by IFT-based tubulin delivery at the MS and DS tips, but capped by the maximal rate) used for results shown in Fig. 5 are 73 and 62 nm s^{-1}, respectively.

Parameter Name	Value
N = the number of IFT-complex in the cilium	200-800 (500)
kinesin-II to OSM-3 ratio per IFT-complex	1:1
(kinesin-II & OSM-3)/dynein per IFT complex	1:1
Maximum number of MS and DS tubulin isotype subunit per IFT-complex	1-15 (2) (MS) 1-15 (3) (DS)
v_{gMS}* & v_{sMS}	80/11-1200/11 nm/s
v_{gDS}* & v_{sDS}	80/13-1200/13 nm/s
f_{cat} & f_{res}	*0.1-0.3/s*

Literature for Supplemental Modeling data

1. Verde, F., Dogterom, M., Stelzer, E., Karsenti, E. & Leibler, S. Control of microtubule dynamics and length by cyclin A- and cyclin B-dependent kinases in Xenopus egg extracts. *J Cell Biol* **118**, 1097-1108 (1992).
2. Evans, J.E. *et al.* Functional modulation of IFT kinesins extends the sensory repertoire of ciliated neurons in *Caenorhabditis elegans*. *J Cell Biol* **172**, 663-669 (2006).
3. Marshall, W.F., Qin, H., Rodrigo Brenni, M. & Rosenbaum, J.L. Flagellar length control system: testing a simple model based on intraflagellar transport and turnover. *Molecular biology of the cell* **16**, 270-278 (2005).
4. Snow, J.J. *et al.* Two anterograde intraflagellar transport motors cooperate to build sensory cilia on C. elegans neurons. *Nature cell biology* **6**, 1109-1113 (2004).
5. Pan, X. *et al.* Mechanism of transport of IFT particles in C. elegans cilia by the concerted action of kinesin-II and OSM-3 motors. *J Cell Biol* **174**, 1035-1045 (2006).
6. Pigino, G. *et al.* Electron-tomographic analysis of intraflagellar transport particle trains in situ. *J Cell Biol* **187**, 135-148 (2009).